PLASMONIC BIOSENSOR DESIGN AND ALTERNATIVE PLASMONIC MATERIALS

A THESIS SUBMITTED TO
THE GRADUATE SCHOOL OF
ENGINEERING AND NATURAL SCIENCES
OF ISTANBUL MEDIPOL UNIVERSITY
IN PARTIAL FULFILLMENT OF THE REQUIREMENTS FOR
THE DEGREE OF
MASTER OF SCIENCE
IN
BIOMEDICAL ENGINEERING AND BIOINFORMATICS

By
Erhan Saatçioğlu
December, 2022

PLASMONIC BIOSENSOR DESIGN AND ALTERNATIVE PLASMONIC MATERIALS

By Erhan Saatçioğlu

09 December 2022

We certify that we have read this dissertation and that in our opinion it is fully adequate, in scope and in quality, as a dissertation for the degree of Master of Science.

Assist. Prof. Dr. Hasan Kurt (Advisor)

Assoc. Prof. Dr. Meral Yüce (Co-Advisor)

Assist. Prof. Dr. Yılmaz Şimşek

Assist. Prof. Dr. Özge Şensoy

Approved by the Graduate School of Engineering and Natural Sciences

Prof. Dr. Yasemin Yüksel Durmaz

Director of the Graduate School of Engineering and Natural Sciences

I hereby declare that all information in this document has been obtained and presented in accordance with the academic rules and ethical conduct. I also declare that, as required by these rules and conduct, I have fully cited and referenced all material and results that are not original to this work.

Signature :

Name, Surname: ERHAN SAATÇİOĞLU

ACKNOWLEDGEMENT

I would like to thank my family for everything. Also, my advisor Hasan Kurt for all the effort he put for me and his guidance not only for these 3 years of master period but also for my 8 years of university life. Lastly, I am grateful to Yasemin Yüksel Durmaz for her support and giving me opportunity to become an academician as Research Assistant in my master period.

Erhan Saatçioğlu

December, 2022

CONTENTS

LIST OF FIGURES

LIST OF SYMBOLS

w : Angular Momentum
Ω : Resistance
λ : Wavelength
E : Electric Field
B : Magnetic Field
H : Magnetic Induction
D : Displacement

ABBREVIATIONS

EOT : Extraordinary Transmission
LSPR : Localized Surface Plasmon Resonance
SLR : Surface Lattice Resonance
SP : Surface Plasmons
SPP : Surface Plasmon Polaritons
SPR : Surface Plasmon Resonance

PLAZMONİK BİYOSENSÖR TASARIMI VE ALTERNATİF PLAZMONİK MALZEMELER

ÖZET

Erhan Saatçioğlu

Biyomedikal Mühendisliği ve Biyoenformatik, Yüksek Lisans

Tez Danışmanı: Dr. Öğr. Üyesi Hasan Kurt

Eş Danışman: Doç. Dr. Meral Yüce

Aralık, 2022

Madde-Işık etkileşimi, zamana bağlı kuantum mekaniğinde özellikle spektroskopinin tanımlanması için en önemli ve çalışılan konulardan birisidir. Madde- Işık etkileşimi iki farklı şekilde açıklanabilir. Bunlardan birincisi klasik yoldur ve şu şekilde açıklar, madde-ışık etkileşimi salınan elektromanyetik alan ile yüklü parçacıkların etkileşimi sonucu oluşur. İkinci yol ise kuantum mekaniğidir ve o da şu şekilde açıklar, maddelerin kuantum durumlarının ışık alanlarıyla eşleşmesiyle oluşur. Bu tez madde-ışık etkileşimlerinin bir dalı olan Plazmonik alanı ile ilgili yazılmıştır. Plazmonik dalı, nanometrik ölçekteki metal-dielektrik, metal-yalıtkan gibi farklı yüzeyler boyunca belirli frekasnalarda ışığın manipülasyonu olarak tanımlanabilir. Bu etkileşimler yüzey plazmon rezonansları, localize yüzey plazmon rezonansları, olağanüstü optik iletim ve yüzey kafes rezonansı gibi farklı teknolojilerle araştırılır. Bu dört teknolojinin birbirleri üzerinde farklı uygulamalar için onları tercih sebebi yapan kendilerine has avantaj ve dezavantajları vardır. Plazmonik alanında yüksek direk akım iletkenlikleri ve düşük omik kayıpları nedeniyle en çok kullanılan malzemeler altın ve gümüştür. Ancak, optik frekanslar, bir electron fermi yüzeyine veya boş iletim bandına hareket ettiğinde meydana gelen bantlar arası geçiş ile ilgili başka bir özellik daha gerektirir. Ayrıca altın ve gümüşün nanofabrikasyonunda ana maddeden farklı morfolojik değişiklikler oluşmasından kaynaklı zorluklar oluşmaktadır. Işığın bu zorlukları ve özellikleri, bilim adamlarını plazmonik alanında kullanmak için yeni malzemeler bulma gereği oluşturmuştur.

Bakır, alüminyum, nikel, platin gibi metaller ve titanium nitrür, hafniyum nitrür and zirkonyum nitrür gibi metal nitrürler plazmonik alanında altın ve gümüşün yerini alacak adaylar olarak incelenmektedir. Bu malzemeler arasından aluminyum, titanium nitrür, hafniyum nitrür ve zirkonyum nitrür; altın ve gümüş ile karşılaştırılmak için seçilip tez boyunca farklı açılardan incelenmiştir. Bu malzemeleri karşılaştırmak için kullanılan parametreler yüzey hassasiyeti, nanodeliğin kalınlığı, nanodeliğin yarıçapı, farklı substratlar ve nanodelik periyodlarıdır. Nanodelikler her malzeme ve parameter için tek tek oluşturulmuş ve simule edilmiştir. Simulasyonlar yapıldıktan sonra çıkan veriler excel ve Origin programları aracılığıyla incelenmiş ve yorumlanmıştır. Sonuçların incelenmesi sonucunda Titanyum Nitrür ve Hafniyum Nitrür'ün performansları göze çarpmıştır.

Anahtar sözcükler: Plazmonik, madde-ışık, elektro-optik

PLASMONIC BIOSENSOR DESIGN AND ALTERNATIVE PLASMONIC MATERIALS

ABSTRACT

Erhan Saatçioğlu

MSc in Biomedical Engineering and Bioinformatics

Advisor: Assist. Prof. Dr. Hasan Kurt

Co-Advisor: Assoc. Prof. Dr. Meral Yüce

December, 2022

Light-matter interaction is the one of the most important and studied topic in time dependent quantum mechanic especially for description of spectroscopy. Light matter interaction can be described in two ways. First one is classic way which explains as ligh-matter interactions are the outcome of the charged particles interaction with oscillating electromagnetic field. Second one is quantum mechanically which explain as coupling of quantum states of the matter with light fields. This thesis focuses on a field of light matter interactions called Plasmonics. Plasmonics can be described as manipulation of light at certain frequencies along different interfaces such as metal-dielectric, metal-insulator in nanometric scale. These interactions are investigated with different technologies like surface plasmon resonances, localized surface plasmon resonances, extraordinary optical transmission, and surface lattice resonance. These four technologies have their own advantages and disadvantages which makes them suitable for different applications. In the field plasmonics mostly used materials are gold and silver due to their high DC conductivities and small ohmic losses. Nevertheless, optical frequencies requires another feature related to interband transition which occurs when an electron moves to fermi surface or empty conduction band. Also, nanofabrication of gold and silver have some challenges like morphological changes. These challenges and features of light make scientist to find new materials to use in plasmonics field.

Metals like copper, aluminum, titanium, nickel, platinum also metal nitrides like titanium nitride, zirconium nitride are studied as candidates to replace gold and silver in the field of plasmonics. Inside these materials’ aluminum, titanium nitride, hafnium nitride and zirconium nitride are chosen and studied to compare with gold and silver. Parameters used to compare these materials are surface sensitivity, thickness of the nanohole, radius of the nanohole, different substrates and period of the nanoholes. Nanoholes are constructed using simulation software for each of the material and each of the parameter. Simulations were made results are extracted and investigated via excel and Origin.

Keywords: Plasmonics, matter-light, electro-optics

CHAPTER 1

1. INTRODUCTION

Light-matter interaction is one of the essential aspects of human perception. A large part of the cerebral cortex of the human brain processes visual data coming from surroundings. However, the structure of our retinas and visual pigments restricts the wavelengths that a human can see to between 390 nm and 750 nm. Also, a human eye cannot differentiate objects smaller than 0.1 mm. Since the beginning of civilization, humankind has always wanted to see things that the eye cannot see. We developed microscopes and telescopes to explore the world around us. The discovery of electromagnetic radiation lets us understand light better and utilize it to see and work on the nanoscale. Plasmonics is a field that uses this information to investigate extraordinary and unique properties of metallic structures on the nanoscale. These investigations and efforts led to the discovery of surface plasmons which are collective light-induced excitations of free electrons of metals. These surface plasmons change the scattering characteristics of the light dramatically. Furthermore, it was seen that this property of the surface plasmons allows the production of much smaller circuitry than the commonly used ones. Metal films with nanoholes demonstrated extraordinary optical transmissions. On the other hand, extensive studies showed some limitations, such as high resistive losses of metals. Plasmonics allowed both real-life applications and exciting scientific research. A small spherical nanoparticle can act as a small antenna that concentrates the light to nanoscale areas, allowing to investigate light-matter interactions beyond the diffraction limit of the light [1].

The global biosensors market was valued at 25.5 billion USD in 2021, and estimation shows a 7.5% annual growth rate between 2021 and 2026. The estimated global market value for 2026 is 36.7 million USD. The main reason for this fast growth is the widespread use of nanotechnology-based biosensors. Significant advances in this field increased use of biosensor in diabetes, POC applications, also COVID-19 pandemic influenced the rapid increase in nanotechnology. The Plasmonics field took advantage of the growing nanotechnology market and its popularity increases yearly. Plasmonics-based biosensors have advantages compared to conventional ones, such as electrochemical biosensors, chromatography, mass sensitive biosensors. These advantages are high reusability, short response time, real-time monitoring, simple sample treatments, minimal electrical component use, and label-free detection [2].

The field of plasmonics mainly uses gold and silver for its application due to their small ohmic losses and high DC conductivity. However, when optical frequencies are considered, there is another problem related to the interband transition. It happens when an electron absorbs a photon to jump to the Fermi surface or an empty conduction band. In addition to interband transitions, metals have some nanofabrication challenges, such as they show different morphologies than the bulk material, which causes a decrease in optical properties. These challenges of metals make them unfavorable for many plasmonic devices [3].

This thesis compares group 4 transition metal nitrides to gold, silver, and aluminum as plasmonic material. Their characteristics under different design aspects have been studied alongside different plasmonics phenomena LSPR, SPR, and EOT. Utilized design parameters for EOT comparison are period of the nanoholes, thickness of the nanohole, radius of the nanohole, surface sensitivity, and different substrates.

CHAPTER 2

2. THEORETICAL PART

2.1. Interaction of EM Radiation with Matter

Light interacts with the metal and couples free electrons of noble elements. This coupling causes free electrons to interact with each other and create collective oscillations known as a plasmon. The field studies how electromagnetic radiation can be concentrated to volumes smaller than the wavelength of the wave called plasmonics. The interaction of metals and electromagnetic radiation can be explained with Maxwell's Equations. Also, this interaction mostly depends on the electronic structure of the metal and the frequency of the radiation. Low frequencies like the microwave or far-infrared electromagnetic waves cannot propagate because metals are highly reflective elements. A neglectable portion of the radiation passes through the metal to a certain distance called the skin depth. In frequencies around the visible range, the dissipation effect becomes substantial, and penetration inside the metal increases, making it hard to analyze how metal works in these frequencies. Lastly, high frequencies around ultraviolet metal demonstrates dielectric properties and let EM radiation. Electronic band structure determines the refractive index and absorption of the metal. Maxwell's equations explain electromagnetic responses;

$$\nabla . D = \rho_{ext} \tag{2.1}$$

$$\nabla . B = 0 \tag{2.2}$$

$$\nabla x E = -\frac{\partial B}{\partial t} \tag{2.3}$$

$$\nabla x H = J_{ext} + \frac{\partial D}{\partial t} \tag{2.4}$$

These equations link the four different fields which are, electric field E, magnetic field B, dielectric displacement D, and magnetic induction H. Besides, ρ_{ext} external charge density and J_{ext} external current density. In addition to these fields, two different fields can be introduced by these equations;

$$D = \varepsilon_0 E + P \tag{2.5}$$

$$H = \frac{1}{\mu_0} B - M \tag{2.6}$$

P is polarization, and M is magnetization. Due to non magnetic field is the topic of this thesis M can be ignored. So, the only P will be considered, and P is about the internal charge density, which is showed as ρ_{int}. If charge conservation is applied $\nabla . J = -\frac{\partial_{\rho_{int}}}{\partial_t}$ which implies;

$$J = \frac{\partial P}{\partial t} \tag{2.7}$$

If the medium is nonmagnetic, isotropic, and linear, it means E and B is proportional to D and H. So, relative electrical permittivity ε and magnetic permeability μ can be used to rewrite **equations 2.5 and 2.6**;

$$D = \varepsilon_0 \, \varepsilon E \tag{2.8}$$

$$B = \mu_0 \, \mu H \tag{2.9}$$

If conductibility σ is introduced for the same media, the relationship between internal current density J and electric field E can be written as;

$$J = \sigma E \tag{2.10}$$

On the other hand, if the medium is not linear, these predictions are not correct. The response of the metal highly depends on the frequency. So, the linear relationship between time and space should be taking account, and it can be generalized as;

$$D(r,t) = \varepsilon_0 \int dt' dr' \varepsilon(r - r', t - t') E(r't') \tag{2.11}$$

$$J(r,t) = \int dt' dr' \sigma(r - r', t - t') E(r't') \tag{2.12}$$

After taking the Fourier transform of these equations in (k,ω) domain, convolution becomes multiplication;

$$D(k,\omega) = \varepsilon_0\varepsilon(k.\omega)E(k,\omega) \tag{2.13}$$

$$J(k,\omega) = \sigma(k,\omega)E(k,\omega) \tag{2.14}$$

Combining **equations 2.5, 2.7 and 2.13** conductivity σ and relative permittivity ε can be linked as;

$$\varepsilon(k,\omega) = 1 + \frac{i\sigma(k,\omega)}{\varepsilon_0\omega} \tag{2.15}$$

In general, relative permittivity is used for optical frequencies. On the other hand, conductivity is used for low frequencies. ε can be showed as $\varepsilon(\omega) = \varepsilon_1(\omega) + i\varepsilon_2(\omega)$. Since it is a complex function of angular frequency w. Nevertheless, due to reflectivity measurements, the complex refractive index of the medium is determined as $\tilde{n}(\omega) = n(\omega) + ik(\omega)$. By using these correlations, relative permittivity can be calculated as;

$$\tilde{n}(w) = \sqrt{\varepsilon(w)} \tag{2.16}$$

k, complex part of the $\tilde{n}(w)$ is named as extinction coefficient, which demonstrates the optical adsorption EM waves passing through a media [4].

2.2. Drude Model

Drude model was introduced in the beginning of 20th century by Paul Drude. The model demonstrates the carrying features of electrons in materials but primarily in metals. In other words, Drude Model aims to explain the resistivity of a conductor by using electron scattering in terms of immobile ions acts as an obstacle to electrons motion. The model assumes that the material has a non-interacting electron cloud and motionless positive particles. Electrons of the metal move until they are bumped with a positive particle when radiation strikes the metal. This collision happens in a specific frequency which is showed as $\gamma = {}^{1}/_{t}$. t stands for the relaxation time of the electron gas, and γ is an order of 100 THz at room temperature. Even though model accepts these assumptions, it gives acceptable results in a wide frequency range. This range goes up to the interband transition of metal. The model does not work the same for all metals. For instance, it works fine for alkali metals until UV frequencies. However, for noble metals, since the validity is limited, it works until optical wavelengths. There is a substantial contribution coming from the bound electrons. These so interband transitions that cause high radiation absorption should be considered. An equation of motion can be obtained by only using free electrons and driving electric field E;

$$m\ddot{x} + m\gamma\dot{x} = -eE \tag{2.17}$$

If a harmonic dependence is assumed for the electric field $E(t) = E_0 e^{-\imath wt}$ also, assuming that steady-state result has same harmonic dependence $x(t) = x_0 e^{-\imath wt}$, x_0 is a complex value.

$$x(t) = \frac{e}{m(w^2 + \imath\gamma w)} E \tag{2.18}$$

$x(t)$ is single electron's displacement, so it creates a single dipole moment which is $p(t) = -ex(t)$. To find the polarization of the system contribution of all n electrons should be considered.

$$P = -nex = -\frac{ne^2}{m(w^2 + \imath\gamma w)} E \tag{2.19}$$

If **equations 2.5 and 2.19** combined vector D becomes.

$$D = \epsilon_0 \left(1 - \frac{w_p^2}{w^2 + \imath\gamma w}\right) E \tag{2.20}$$

In this equation plasma frequency of the gas which is $w_p^2 = \frac{ne^2}{\epsilon_0 m}$ is added. The equation in the parentheses in the above equation separates real and imaginary parts, and it's from Drude model.

$$\epsilon(w) = 1 - \frac{w_p^2}{w^2 + \imath\gamma w} = \left(1 - \frac{w_p^2}{w^2 + \gamma^2}\right) + \imath\left(\frac{w_p^2 \gamma}{w(w^2 + \gamma^2)}\right) = \epsilon_1(w) + \imath\epsilon_2(w) \tag{2.21}$$

This model gives good results for frequencies bigger than plasma frequency at higher frequencies like $w \gg \; w_p$ above equation gives $\epsilon(w) \; \rightarrow \; 1$. Since d band electrons are close to Fermi surface for real metals, especially in noble ones, polarization is greater, and the equation gives false results. To prevent that, $P_\infty \; = \; \epsilon_0(\epsilon_\infty - 1)$ can be added to the equation. Thus, P shows the polarization of the free electrons, and the equation becomes [4].

$$\epsilon(w) = \left(\epsilon_\infty - \frac{w_p^2}{w^2 + \; \gamma^2}\right) + \iota\left(\frac{w_p^2\gamma}{w(w^2 + \; \gamma^2)}\right) \tag{2.22}$$

2.3. Lorentz-Drude Model

Below the Fermi surface and above the frequency threshold, radiation excites bounded d electrons to upper bands causing powerful adsorption and a race between s and d electrons. To see the effect of these bounded electrons, another term should be added to the **equation 2.17**;

$$m\ddot{x} + m\gamma\dot{x} + mw_0^2x = \; -eE \tag{2.23}$$

In this way, bounded electrons which act as oscillators with their resonance frequency w_0 considered, and the interband transition effect is included into consideration. This resonance frequency represents a specific interband transition with hw_0 energy. If there are more interband transitions, number of the equations will be the same as those with their resonance frequency. Every single equation ends up with a Lorentz-oscillator like

$$\frac{A_i}{w_i^2 - \; w^2 - \iota\gamma_i w} \tag{2.24}$$

In this equation w_i is the resonance frequency of the i-th interband transition, and w is the radiation frequency. If the number of transitions is N, the dielectric function becomes

$$\epsilon(w) = \; \epsilon_\infty - \frac{w_p^2}{w^2 + \iota\gamma w} + \sum_{i=1}^{N}\frac{A_i}{w_i^2 - \; w^2 - \iota\gamma_i w} \tag{2.25}$$

By using the link between ϵ and σ, the dielectric function becomes [4].

$$\epsilon(w) = \epsilon_\infty - \frac{\iota\sigma}{\epsilon_0 w} + \sum_{i=1}^{N} \frac{C_i}{w^2 + \iota A_i w + B_i} \tag{2.26}$$

2.4. Plasmon Polaritons

2.4.1. Volume plasmons

Neglecting the interband effect shows that metals are transparent to radiation. So, the real part of $\epsilon(w)$ is dominant, and the imaginary part becomes ignorable.

$$\epsilon(\omega) \sim \epsilon_1(w) = 1 - \frac{w_p^2}{w^2} \tag{2.27}$$

After combining Maxwell’s equations with the above equation, another wave equation related to the transparency regime supporting propagating waves was found.

$$w^2 = w_p^2 + k^2c^2 \tag{2.28}$$

Importance of the w_p can be found by looking collective oscillation of electron gas against ion cores in a plasma slab with a positive background. The collective movement of the electron gas causes a surface charge density at the boundaries of the slab. This surface charge density creates an electric field. As a result, a restoring force applies to transpose electrons. In other words, free oscillation of the electron sea has a natural frequency which is named plasma frequency w_p. Volume plasmon is the quanta of these charge oscillations. Volume plasmons can only be excited with particle impact because they do not couple in transverse electromagnetic waves [4].

2.4.2. Surface plasmon polaritons

Surface plasmon polaritons are electromagnetic excitations that occur on the surface between metal and dielectric material. This interaction on metallic surfaces demonstrates a notable improved optical near-field. Research and development efforts on SPP-based devices are growing rapidly due to their unique features and their application in many fields such as data storage, biosensing, and solar cells.

To find spatial field profile and dispersion of propagating waves, wave equations should be used. Wave equations can be used when apparent equations for electric and magnetic field is found. After finding these equations, it can be seen that there are two distinct solutions. The first one is transverse magnetic (TM or p), where E_x, E_z, and H_y are nonzero, the second one is transverse electric, where H_x, H_z, and E_y are nonzero. However, TM solution is used for the SPP case because SPP does not exist in TE polarization. The wave equation for the TM mode is,

$$\frac{\partial^2 H_y}{\partial z^2} + (k_0^2\varepsilon - \beta^2)H_y \tag{2.29}$$

Using the TM solutions for both half-spaces.

$$H_y(z) = A_2 e^{i\beta x} e^{-k_2 z} \tag{2.30}$$

$$E_x(z) = iA_2 \frac{1}{w\varepsilon_0\varepsilon_2} k_2 e^{i\beta x} e^{-k_2 z} \tag{2.31}$$

$$E_z(z) = -A_1 \frac{\beta}{w\varepsilon_0\varepsilon_2} e^{i\beta x} e^{-k_2 z} \tag{2.32}$$

for $z > 0$,

$$H_y(z) = A_1 e^{i\beta x} e^{-k_1 z} \tag{2.33}$$

$$E_x(z) = iA_1 \frac{1}{w\varepsilon_0\varepsilon_1} k_2 e^{i\beta x} e^{-k_1 z} \tag{2.34}$$

$$E_z(z) = -A_1 \frac{\beta}{w\varepsilon_0\varepsilon_1} e^{i\beta x} e^{-k_1 z} \tag{2.35}$$

Continuousness of H_y and $\varepsilon_i E_z$ at the surface requires $A_1 = A_2$ so,

$$\frac{k_2}{k_1} = -\frac{\varepsilon_1}{\varepsilon_2} \tag{2.36}$$

Surface waves occur only when dielectric permittivities of the materials signs are opposite to each other. So, H_y must fulfill the TM mode wave equation so,

$$k_1^2 = \beta^2 - k_0^2\varepsilon_1 \quad \textbf{(2.37)}$$

$$k_2^2 = \beta^2 - k_0^2\varepsilon_2 \quad \textbf{(2.38)}$$

Using **equation 2.36** with these equations dispersion relation of SPPs between two half-space found as;

$$\beta = k_0\sqrt{\frac{\varepsilon_1\varepsilon_2}{\varepsilon_1 + \varepsilon_2}} \quad \textbf{(2.39)}$$

This equation applies to both conductors with attenuation and without attenuation [4].

2.4.3. Localized surface plasmons

Localized Surface Plasmon occurs when light with a wavelength of smaller or comparable to nanoparticle excites the plasmon. Suppose a small metal nanoparticle is irradiated with a light electric field. In that case, conduction electrons oscillate, which causes electrons to move away from their original position. The frequency of this oscillation is affected by some parameters, such as the size of the charge distribution and density of the electrons. This replacement causes a restoring force from Coulombic attraction between electrons and nuclei. Thanks to restoring force which is a result of curved surface EM waves directly excites localized plasmon resonance. The shape and size of nanoparticles determine the resonance frequency.

In 1908 Gustav Mie introduced Mie theory, which explains spherical multipole partial waves scattering by using a single non-interacting spherical particle. For well-separated nanoparticles, Mie’s solution for Maxwell’s equations can be used to find extinction cross-section [5].

$$C_{ext} = \frac{24\pi^2 R^3 \varepsilon_m^{3/2} N}{\lambda \ln(10)} \frac{\varepsilon_i}{(\varepsilon_r + X\varepsilon_m)^2 + \varepsilon_i^2} \quad \textbf{(2.40)}$$

2.5. Excitation of Surface Plasmons

2.5.1. Prism coupling

SPPs cannot be excited directly on the metal-dielectric interface due to propagation constant β is greater than wave vector k of light. Projection in the interface can be found as,

$$k_x = k \sin \theta \tag{2.41}$$

θ is the angle of the photons crashing to the interface, is smaller than propagation constant β and prevents phase-matching. To get the phase-matching, prism couplers are used. Prism couplers consist of three layers insulator-metal film-insulator. These insulators have different dielectric constants. Interface between insulator with higher dielectric constant ε cause beams to usually reflects in the form of prism and metal has in-plane momentum of,

$$k_x = k\sqrt{\varepsilon} \sin \theta \tag{2.42}$$

This momentum allows SPPs to excite in the interface of the insulator with lower dielectric constant and metal.

There are two different types of prism coupling; one of them is the Kretschmann method. In this method, on top of a glass prism, a thin metal film is evaporated. EM waves hitting the glass part with a higher angle than its critical angle excited the SPPs in the metal-air interface. On the other hand, the second method is known as Otto configuration. In this one, there is an air gap between prism and metal film. SPPs happens due to the tunneling effect in the air-metal interface since in the prism-air interface, total internal reflection occurs. Mostly, Otto configuration is preferred because there is no contact with the metal surface [4].

2.5.2. Grating coupling

Another way of overcoming $\beta > k$ is creating holes or grooves on the surface of the metal with lattice constant a. Phase-matching occurs when the given formula applies,

$$\beta = k \sin \theta \ \pm vg \qquad \textbf{(2.43)}$$

In this equation, $g = \frac{2\pi}{a}$ is gratings reciprocal vector. Dielectric materials can also be used instead of milling gratings onto the metals. The shape of these grating affects SPPs and can be used for focusing. Sufficiently deep gratings cause substantial changes in SPP dispersion because modulation becomes significant. For metallic gratings with a groove depth of 20 nm, observable band gaps occur [4].

2.6. Common Refractometric Sensing Schemes in Nanoplasmonic Sensing

Plasmonics is a well-recognized research and development area that works on different features of surface plasmon based technologies. The scientist's interest in surface plasmons had started to increase in 1990. After that, it increased dramatically. However, the beginning of the research done about the surface plasmons dates back to the beginning of the 1900s. In 1902 a scientist named Robert Williams Wood observed anormal attenuation in the light reflected from a metallic grating. Wood did not name the phenomena as surface plasmon, but it can be said grating’s periodic structure caused the phenomena. Another scientist named Maxwell Garnett developed the theory of effective dielectric constant, allowing to find the color of glasses containing metallic particles. Mie introduced an electromagnetic theory that explains light absorption and scattering features when they hit a spherical particle with random size. This study is the basis of localized surface plasmons, which will be discussed in the coming section. Using prisms to excite surface plasmons was introduced by Andreas Otto in 1968, and this prism was named attenuated total reflection (ATR). In addition, in the same year, Kretschmann and Raether demonstrated another configuration for ATR. Applying this technology to an optical sensor was shown in 1980 by Claes Nylander [6].

2.6.1. SPR based sensing

The behavior of surface plasmons is directly dependent on dielectric features of the metal/dielectric interface background. This dependence allows SPR to be utilized in biochemical reactions close to the surface. SPR sensing technology has four different classes, which are angular, intensity-modulated, and wavelength systems. SPRs are excited with a light wave of different wavelengths in a wavelength system and reflected light is observed. In an intensity-modulated system, light is adjusted to a specific angle and wavelength to observe the intensity of this light. Even though an intensity-modulated system demonstrates lower performance, it is widely used, especially for SPR imaging technologies. Lastly, monochromatic light is used in an angular scanning system with different angles onto a metallic surface. It excites the plasmons on the surface of the metal. Absorption of the light is observed by looking at the dip in the spectrum of reflected light. The angular scanning method is the most sensitive and commonly used in these three different systems [7].

Prism coupling in Kretschmann configuration is the most utilized method to excite SPPs. Total reflection occurs at the base of the prism it causes the formation of surface plasmons. The surface plasmons absorb some part of the light energy that moves through the surface of the metal film at a specific angle.

$$\theta_{SPR} = \sin^{-1}\sqrt{\frac{\varepsilon_m \varepsilon_d}{\varepsilon_p(\varepsilon_m + \varepsilon_d)}} \qquad \textbf{(2.44)}$$

$\varepsilon_m, \varepsilon_d, and\ \varepsilon_p$ are dielectric constants of metal, dielectric, and prism. Due to this, reflectance can be seen in angular scanning. The refraction index of the surface is a very important factor that affects the SPR angle. These changes in the SPR angles cause alterations in intensity or placement of SPR minimum angle. So, if a linked or adsorbed molecules surface of the sensor, it changes the refractive index, leading to a change in the SPR angle [8].

Since the concentration of the molecules is very low in biological systems sensor to analyze these molecules needs to be very sensitive. SPR-based sensors demonstrate high sensitivity for biological systems. This makes them used widely for immunosensors, especially for the sensing of antigens by linking antibodies to the surface of SPR sensors. On the other hand, there are some limitations of SPR sensing. One example is that they may cause cross sensitivity and false positive response because some analytes can bind to molecules on the sensor's surface.

SPR technology is used in many fields such as material characterization, medical diagnosis, food quality, pharmaceutical. In medical diagnosis, SPR technology is contributed significantly with its high sensitivity and reproducibility and is also label-free and lets real-time monitoring. In addition, it allows surface alterations with different approaches so improvements can be made to lower the detection limits. Another critical point in medical diagnosis is the detection of biomarkers. Using surface plasmons, multiplexed systems such as surface plasmon resonance imaging are developed to detect multiple DNA, RNA, or proteins with only one electrode. In the food quality field, SPR technology is utilized to detect bacterial contaminations, pathogens, and toxins. Lastly, in the pharmaceutical area, SPR is used for different purposes. These purposes can be listed as, investigating the binding features of reactants, determining affinity constants with real-time monitoring, finding binding and unbinding rate of the molecules, quantifying the concentration of the interacting reactants [9].

2.6.2. LSPR based sensing

Localized surface plasmon resonance consists of metallic nanostructured particles smaller than the incident light. They confine non-propagating harmonic oscillations of free electrons in the interface of the dielectric and metal. In other words, peaks of the spectrum are sensitive to the interface of metal and dielectric; this way, it allows to recognize the biomolecules [10]. LSPR is known as one of the best techniques utilized in biotechnology and biosensor fields. The main advantages of LSPR based biosensors are good reproducibility, low cost, and easy setup, high sensitivity to refraction index changes, label-free, real-time monitoring using microfluidic systems. In addition, LSPR shifts sometimes can be so significant that they can be observed with the naked eye. LSPR shows better surface sensitivity compared to SPR. LSPR has lower field decay length, making an LSPR based sensing system analyze analytes close to their surfaces without the interference of further molecules. Also, LSPR has more potential for miniaturization and multiplex systems since it has very short evanescent field decay. Utilizing a high number of microfluidic parallel paths lets real-time monitoring of independent reading sites. These advantages make LSPR is a suitable technique to use in a variety of fields like SPR. Some examples of these fields are food safety, medical diagnosis, drug screening, and point-of-care applications.

Mie’s solution can explain the scattering and absorption of light on the spherical particles to Maxwell’s equations. The solution introduces a relation between the scattering cross-section of metal nanoparticles and the sum of the absorption cross-section called extinction cross-section.

$$\sigma_{ext} = \sigma_{abs} + \sigma_{sca} \tag{2.45}$$

For small particles, the solution becomes,

$$\sigma_{ext} = 9\frac{w}{c}\varepsilon_{3/2} V_0 \frac{\varepsilon_2(w)}{[\varepsilon_1(w) + 2\varepsilon_m]^2 + \varepsilon_2(w)^2} \tag{2.46}$$

$V_0 = \left(\frac{4\pi}{3}\right) R^3$, w is the angular frequency of the radiation of the extinction, ε_m is the dielectric constant of the medium around the metal nanoparticle, ε_1 and ε_2 are real and imaginary parts of the dielectric constant of the metal nanoparticle.

The shape of the nanoparticles is an essential factor for the sensitivity of the LSPR signal. The nanoparticle shape varies according to the need, some shapes are nanodiscs, nanospheres, nanorods, and nanopyramids. The extension of Mie theory called Gans theory explains the scattering features of nanospherical nanoparticles for both oblate and prolate ones. For prolate particles, absorption cross-section is,

$$\sigma_{abs} = \frac{w}{3c}\varepsilon_m^{3/2} V \sum_j \frac{\left(1/P_j^2\right)\varepsilon_2}{\left[\varepsilon_1 + \left\{(1-P_j)/P_j\right\}\varepsilon_m\right]^2 + \varepsilon_2^2} \tag{2.47}$$

j stands for dimensions of the particle, P_j has three features P_A, P_B, P_c which are the depolarization constants for each axis of the particle. ε_1 and ε_2 are altered anisotropically by the depolarization constants, and LSPR peak frequency becomes,

$$P_A = \frac{1 - e^2}{e^2}\left[\frac{1}{2e}\ln\left(\frac{1+e}{1-e}\right) - 1\right] \tag{2.48}$$

$$P_B = P_C = \frac{1 - P_A}{2} \tag{2.49}$$

e includes the aspect ratio R and shows as,

$$e = \left[1 - \left(\frac{B}{A}\right)^2\right]^{1/2} = \left(1 - \frac{1}{R^2}\right)^{1/2} \tag{2.50}$$

Since LSPR based sensors detect shifts in the spectrum by the changes in the localized refractive index around the surrounding area of the nanoparticle, the peak in the LSPR depends on the dielectric features of surrounding media. To prove this relation Drude model with the neglected interband effect can be used **equation 2.27** Under resonance condition, it becomes,

$$w_{max} = \frac{w_p}{\sqrt{2\varepsilon_m + 1}} \tag{2.51}$$

w_{max} is the frequency of the LSPR peak. By combining $\lambda = \frac{2\pi c}{w}$ and $\varepsilon_m = n^2$ with the above equation, it becomes,

$$\lambda_{max} = \lambda_p \sqrt{2n_m^2 + 1} \tag{2.52}$$

λ_{max} is the wavelength of the LSPR peak and λ_p is the plasma frequency of the bulk material. This relation between the refractive index and the wavelength of the LSPR peak can be used to get high sensitivity for molecular-level applications [11].

2.6.3. EOT based sensing

Transmission of light when it passes through holes with a diameter smaller than the light shows a higher magnitude than the expected one in the classical aperture theory. This unusual phenomenon was introduced in 1988 by Ebbessen and is called extraordinary optical transmission (EOT). Ebbessen and his friends also observed more light transmitted than the real amount coming to the hole area, making the material look more transparent than it normally is. This phenomenon was seen for gold and silver, and it did not show the same effect for the rest of the metals. After that, EOT becomes a popular research area due to its importance and its potential to be used in many fields such as optical data storage, chemical sensors, biosensors, integrated photonics, nanolithography [12].

EOT depends on the distance between the nanoholes on the metal surface, this distance is called periodicity. Also, the nanoholes' ratio of depth and diameter determines the full-width half maxima of the transmission peaks. According to Ebbessen, when the momentum of the surface plasmons reaches the momentum of the incident photon, SPs get excited and their demonstrated as,

$$k_{sp} = k_x \pm nG_x \pm mG_y \tag{2.53}$$

k_{sp} is surface plasmon wavevector, $k_x = \left(\frac{2\pi}{\lambda}\right)\sin\theta$ is a constituent of the photon's wavevector in the plane of the grating, $G_x = G_y = \frac{2\pi}{a_0}$ are grating momentum wavevectors of square nanohole array. There are different modes for nanoholes which are square array and hexagonal arrays. Dispersion relation of these array's resonant peaks shown as,

$$\lambda_{EOT} \cong \frac{\Lambda}{\sqrt{i^2 + j^2}}\sqrt{\frac{\varepsilon_d\varepsilon_m}{\varepsilon_d + \varepsilon_m}} \tag{2.54}$$

$$\lambda_{EOT} \cong \frac{\Lambda}{\sqrt{\frac{4}{3}(i^2 + ij + j^2)}}\sqrt{\frac{\varepsilon_d\varepsilon_m}{\varepsilon_d + \varepsilon_m}} \tag{2.55}$$

Λ is period, ε_d and ε_m are dielectric constant of dielectric medium in the interface and metal, i and j are diffraction orders. This relationship of dispersions with a wavelength of the resonant modes of SPPs lets finding resonance wavelength of plasmonic nanohole arrays

$$S_B = \frac{d\lambda_r}{dn} = \frac{d\lambda_r}{dn_{spp}}\frac{\partial n_{spp}}{\partial n} = \frac{\frac{\partial n_{spp}}{\partial n}}{\left(\frac{\sqrt{i^2 + j^2}}{\Lambda} - \frac{dn_{spp}}{d\lambda}\right)} \tag{2.56}$$

By increasing the period of the nanohole array system, resonance wavelength can be scaled. However, dominant resonance modes will occur in the spectrum because of the diffraction orders. Since period and diffraction order mode is the denominator for EOT, it shows an order lower refraction index sensitivity than SPR. On the other hand, EOT with a classic geometry demonstrates higher sensitivity comparing to commonly used nanodiscs. In addition, EOT does not need polarized light and complicated optical instruments to excite surface plasmons; also, evanescent field decay of it is shorter than the SPR. Lastly, EOT shows higher field confinement than SPR since field enhancements happen on the edges and its geometry allows better detection results of large analytes such as viruses, cells, and bacteria than LSPR [13].

2.6.4. SLR based sensing

Nonlinear optical conversion became available by the studies done on nonlinearity of metallic nanoparticles. These finding inspired scientist for the make research on nonlinear optics with controlled nonlinearity by changing the geometry of the nanoparticle complexes. Furthermore, it is found that array of similar particles with controlled lattice symmetry, spacing and orientation can modify single nanostructure secondharmonic. Better results for the control of the optical response can be obtained due to lattice complexes at the photonic regime of the secondharmonics [14].

Coupled dipole approximation (CDA) is used to predict diffraction of coupled resonances and explanation of their fundamental functions. To explain these phenomenon N nanoparticles whose positions and polarizations are α_i and r_i. Dipole P_i is applied to every particle and it is found as $P_i = \alpha_i E_{loc,i}$. $E_{loc,i}$ is the local field of every particles position. $E_{inc,i}$ and $E_{dipole,i}$ are sum of the incident field and other fields produced by other dipoles. Field can be found as for the given wavelength λ,

$$E_{loc,i} = E_{inc,i} + E_{dipole,i} = E_0\, exp(ik.r_i) - \sum_{j=1}^{N} A_{ij}.P_j (i = 1,2, \ldots, N), \qquad j \neq i \tag{2.57}$$

E_0 is amplitude and $k = {}^{2\pi}/_{\lambda}$ is wavenumber of the incident wave. A_{ij} dipole interaction matrix can be showed as,

$$A_{ij}.P_j = k^2\, exp(ik.r_{ij}) \frac{r_{ij}X(r_{ij}\, XP_j)}{r_{ij}^3} + exp(ik.r_{ij})(1 - ik.r_{ij}) \frac{[r_{ij}^2 XP_j - 3r_{ij}(r_{ij}.P_j)]}{r_{ij}^5} \tag{2.58}$$

r_{ij} is a vector from dipole i to dipole j. Analytical solution for the **equation 2.58** can be found for infinite array of particles by taking induced polarization of the each particle is same and α_S. Each particles P can be found as,

$$P = \frac{E_0}{{}^{1}/_{\alpha_S} - S} \tag{2.59}$$

S is the dipole sum. One particle's extinction cross section can be found as,

$$C_{ext} = 4\pi k \; Im(P/E_0) \tag{2.60}$$

S can be found when the wavevector is perpendicular to the plane of the array,

$$S = \sum_{j\#1} \left[\frac{(1 - ik.r_{ij})(3cos^2\theta_{ij} - 1)exp(ik.r_{ij})}{r_{ij}^3} + \frac{k^2 sin^2\theta_{ij} exp(ik.r_{ij})}{r_{ij}} \right] \tag{2.61}$$

θ_{ij} is the angle between r_{ij} and direction of the polarization.

SLR only needs 50 particles to have narrowing of the plasmonic resonance. SLRs are the result of interaction of light and nanoparticles. SLRs are observed in asymmetric environments eventhough symmetric environments help them greatly. 300 in near infrared and 500 in mid infrared can be achieved by long SLR wavelengths because it causes higher resonance quality. SLRs have stronger field enhancement than LSPR, cause no refraction in some cases and have very narrow widths of plasmon resonances.

2.7. Alternative Plasmonic Materials

Fast grow rate of the plasmonic field make it utilized for many applications and many different research areas. From the first days of the plasmonic are metals are used for maneuvering SPs. Metals are act like antennas to create electric field form the light. For instance, detecting the changes in the dielectric media of sensors and for routing or confining the light beyond conventional diffraction limits. Light can be manipulated by changing the size, shape and spacing of nanostructures. These aspects of plasmonics make it useful for many different fields such as, chemical, and biochemical sensors, nanophotonic circuits, surface enhanced spectroscopy, optical trapping and super resolution imaging [15].

2.7.1. Noble metals

Considering all the metals in the periodic table noble metals attracted much more interest than the rest of the metals for plasmonic applications. There are several reasons for them to be chosen. First of all, they have small ohmic losses and high DC conductivity [3]. Also, for their high performance as plasmonic material due to their permittivities. There are two parts in the permittivities of the materials, real part and the imaginary part. The real part represents how strong polarization the material shows when it is induced by an external electric field. Dielectric media and the reel part of the permittivity give the resonance frequency. On the other hand, imaginary part represents damping of the oscillation of the surface plasmons and energy losses. The noble metals have negative real part and small imaginary part. Negative real part allows surface plasmons to occur in the visible range besides low imaginary part allow LSPRs to be strong and cause large near field enhancement. Gold and silver are the most commonly used noble metals for plasmonic applications. Gold is mostly used for low frequencies due to being physically and chemically stable [15].Besides this feature there are many advantages of gold such as biocompatibility, its surface is easy to functionalize with organic and biological analytes, suitable optical properties link to SPs. Especially, gold nanoparticles have many polarizable conduction electrons which is preferred interaction for nonlinear optical phenomena [16]. On the other hand, silver is less used but shows better results due to its strong LSPRs features over a wide range of wavelength. Besides, silver has higher refractive index sensitivity and dissipate less [15]. Although all these advantages of noble metals, they have some disadvantages that make researchers to study for different plasmonic materials. Some of these disadvantages are they have high interband transition losses, they have some nanofabrication challenges especially when they used as thin films, for silver degradation in air is another big problem [3].

2.7.2. Other metals

Noble metals especially gold and silver are the mostly used materials for plasmonic applications. However, some other metals are started take interest and studied as alternative to noble ones. These metals are Copper (Cu), Aluminum (Al), Nickel (Ni), Titanium (Ti) and Iron (Fe). Copper had more interest than the other ones due to it is cheap and can be found in nature with excess amounts. However, copper degrade with air like silver which makes it bioincompatible. Furthermore, aluminum draw attention for plasmonic applications because of its favorable dielectric features. Its negative permittivity caused by its large plasma frequency goes down to 100 nm, which makes aluminum to potential material for ultraviolet plasmonic applications. Also, like copper it can be found in nature easily and it has low cost. Besides, it demonstrates strong local field enhancement, and it is compatible for optoelectronic applications [17].

2.7.3. Metal nitrides

Advances in the Plasmonics and Nanoplasmonic field such as high-temperature applications, light harvesting, active plasmonics make the field open to new materials and diminishes the realm of gold and silver. Besides, other metals than the noble ones metal nitrides demonstrates promising results for plasmonic applications. They show resemblance with gold and also they are refractor materials which means they can resist to high temperatures. For example, melting point of the gold is 1064 °C on the other hand TiN has 2930 °C and ZrN has 2980 °C melting points. Besides real part of the permittivity of nitrides is smaller than the gold and silver in the visible spectrum but losses are almost equal which is another reason for nitrides to become preferable for plasmonic applications [18].

CHAPTER 3

3. EXPERIMENTAL PART

Materials that compared in this thesis are chosen from various articles (Ag, Au, Al, HfN, TiN, ZrN). Two different titanium nitride and zirconium nitride were used to have a better understanding. For Ag and Al chosen refractive index and extinction coefficient values were already exist in the simulation program Lumerical however, for the rest of the materials data were imported from the given articles to the Lumerical. Data of the material were compared with the FDTD model of the Lumerical to check if there is wrong value. If the models are matched simulations were started.

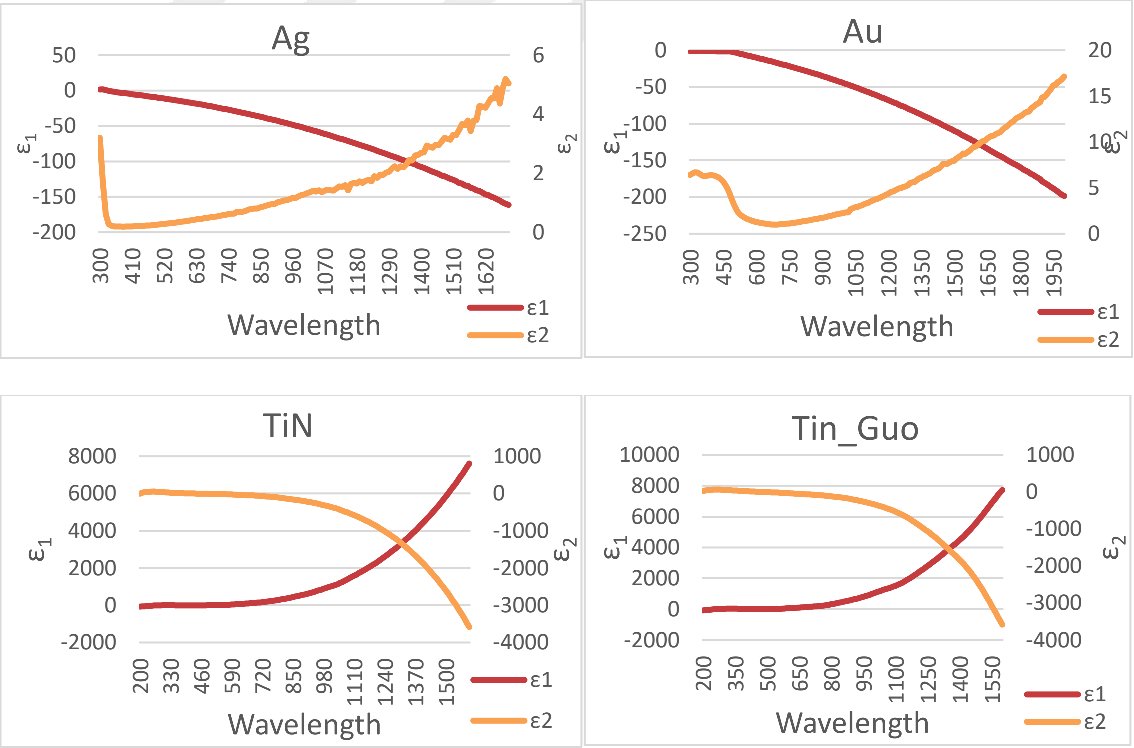

Figure 3.1: Real and Imaginary parts of chosen materials (Ag,Au,TiN).

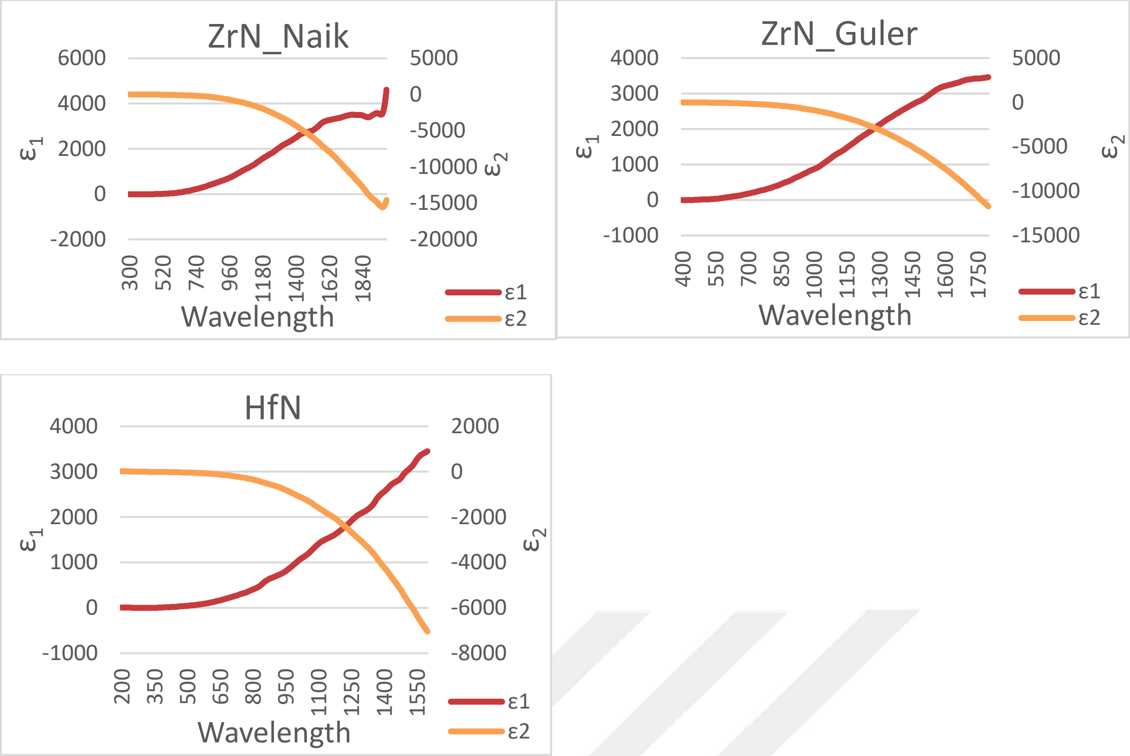

Figure 3.2: Real and Imaginary parts of chosen materials (ZrN,HfN).

Fused silica was chosen as substrate since it is commonly used for plasmonics application, and its refractive index was set as 1.45 as average value for fused silica. On top of the substrate 10 nm of titanium layer was placed to remove undesired propagation of the light between layers. Then, chosen materials are placed with different thicknesses which is mentioned in the coming pages. Nanoholes were created with different diameters and different periods. After the test object is created source is placed on top of the object and detector was placed under the object to measure transmitted light. In order to reduce the simulation times only quarter of the simulated region was investigated in the simulations, since it’s a circle same amount will be transmitted from every quarter of the circle.

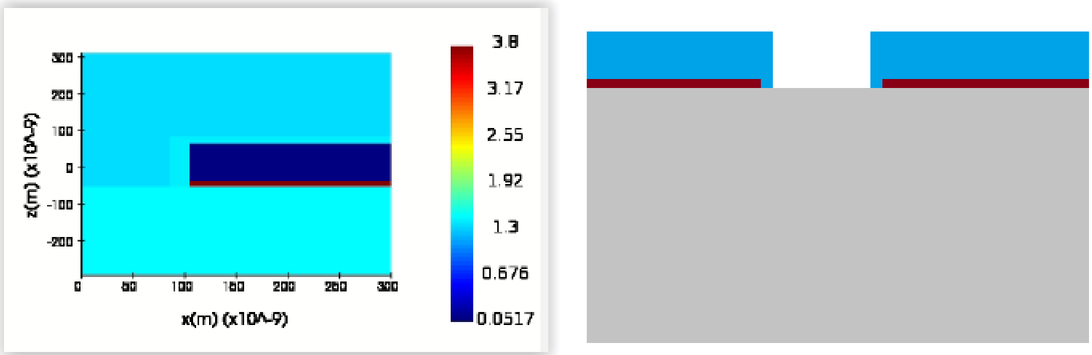

Figure 3.3: Index preview and Illustration of a nanohole.

Different parameters were investigated for each of the materials. These parameters are nanohole sensitivity, thickness of the material, period of the nanoholes, diameter of the nanoholes, minimum hole depth and gap between material and substrate finally refractive index of the substrate.

Nanohole Sensitivity, background index values were changed to see how does nanoholes respond to changes in the refractive index of the surface. Utilized background index values are 1,33; 1,4; 1,45; 1,5; 1,55.

Period of the Nanoholes, period change causes shifting in the transmitted light in the wavelength. To see these changes period values were changed with these values; 400 nm, 500 nm, 600 nm, 700 nm, 800 nm.

Thickness of the Material, thickness changes the amount of transmitted light. To see which thickness, give the best result for the materials, different thickness values were used. These values are 10 nm, 30 nm, 50 nm, 70 nm, 90 nm, 110 nm.

Diameter of the Nanoholes, it both effects the transmitted light and width of the light. Utilized diameter values are 50nm, 75 nm, 100 nm, 125 nm, 150 nm.

Minimum Hole Depth, to see the effect of the hole depth, different depth values were utilized. These values are 50 nm, 70 nm, 90 nm, 110 nm, 130.

CHAPTER 4

4. RESULTS AND DISCUSSION

4.1. SPR Results

4.1.1. Results for silver (Ag)

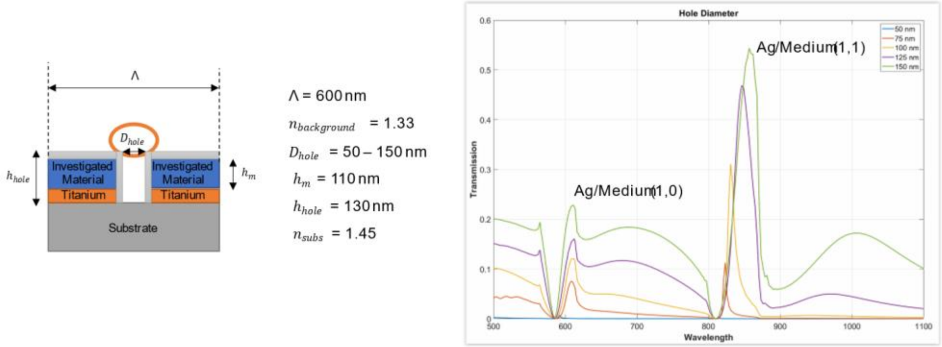

Figure 4.1: Hole diameter simulation results for Ag. Diameter values were chosen as 50 nm, 75 nm, 100 nm, 125 nm, 150 nm.

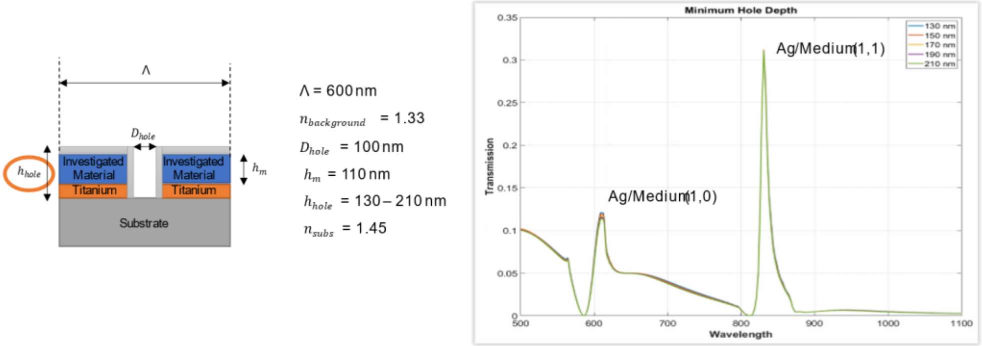

Figure 4.2: Hole depth simulation results for Ag. Depth values were chosen as 130 nm, 150 nm, 170 nm, 210 nm.

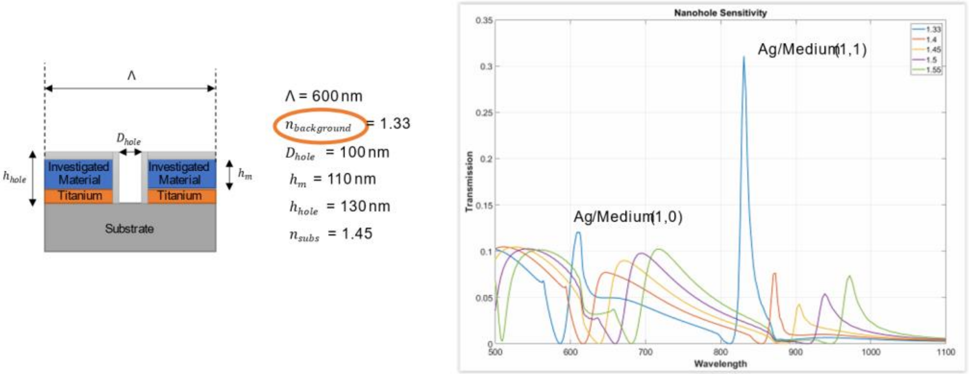

Figure 4.3: Nanohole sensitivity results for Ag. Background index values were chosen as 1.33, 1.4, 1.45, 1.5, 1.55.

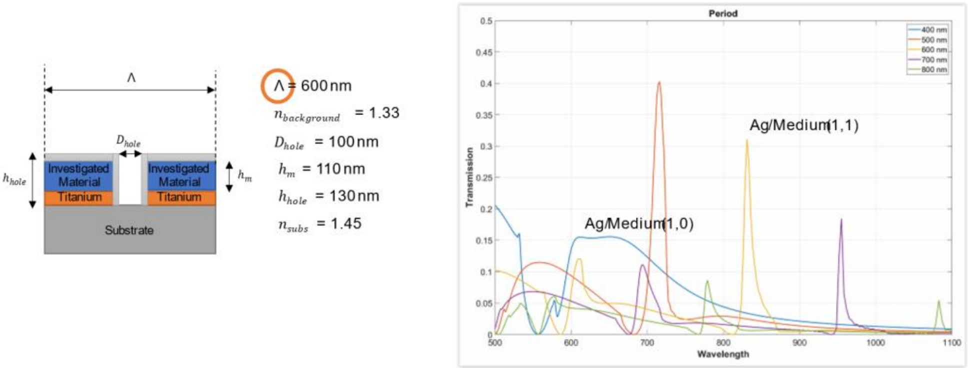

Figure 4.4: Period results for Ag. Period values were chosen as 400 nm, 500nm, 600 nm, 700 nm, 800 nm.

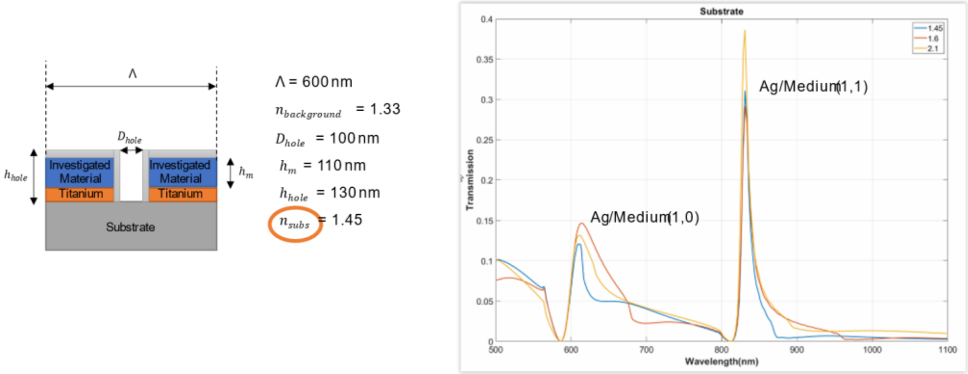

Figure 4.5: Substrate results for Ag. Substrate indexes were chosen as 1.45, 1.5, 2.1.

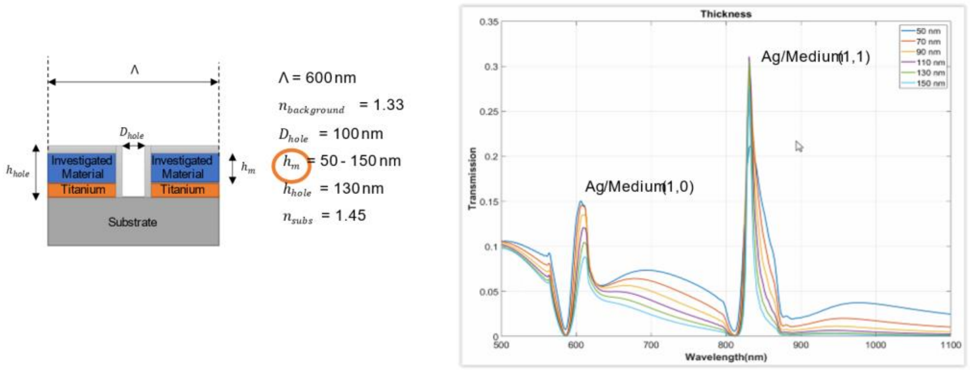

Figure 4.6: Thickness results for Ag. Thickness values were chosen as 50 nm, 70 nm, 90 nm, 110 nm, 130 nm, 150 nm.

4.1.2. Results for gold (Au)

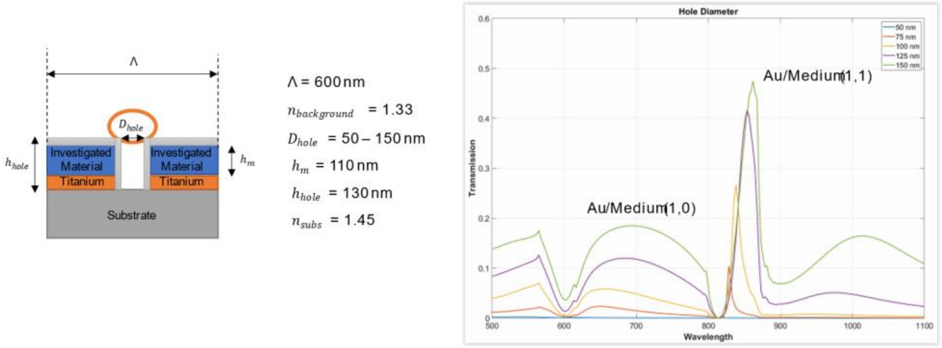

Figure 4.7: Hole diameter simulation results for Au. Diameter values were chosen as 50 nm, 75 nm, 100 nm, 125 nm, 150 nm.

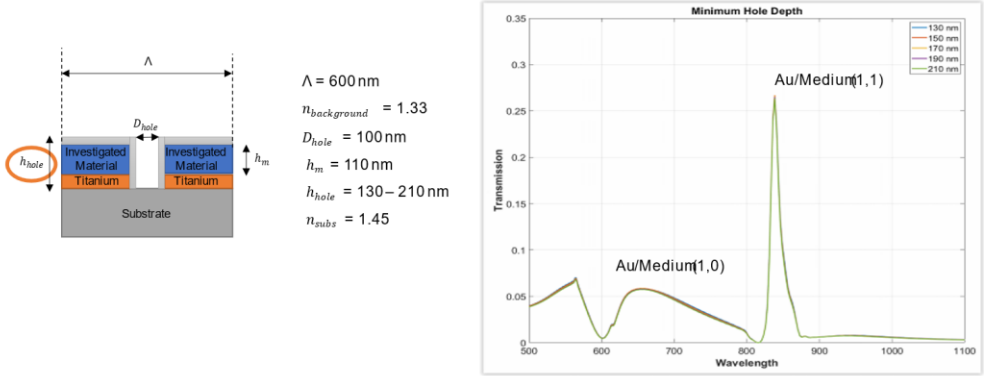

Figure 4.8: Hole depth simulation results for Au. Depth values were chosen as 130 nm, 150 nm, 170 nm, 210 nm.

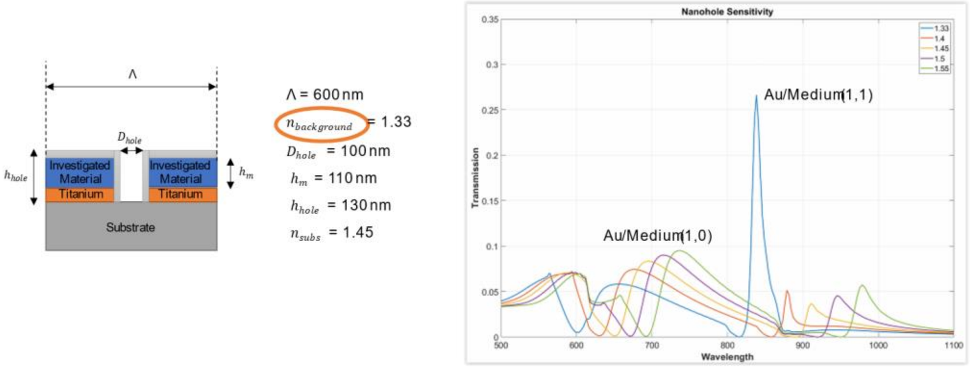

Figure 4.9: Nanohole sensitivity results for Ag. Background index values were chosen as 1.33, 1.4, 1.45, 1.5, 1.55.

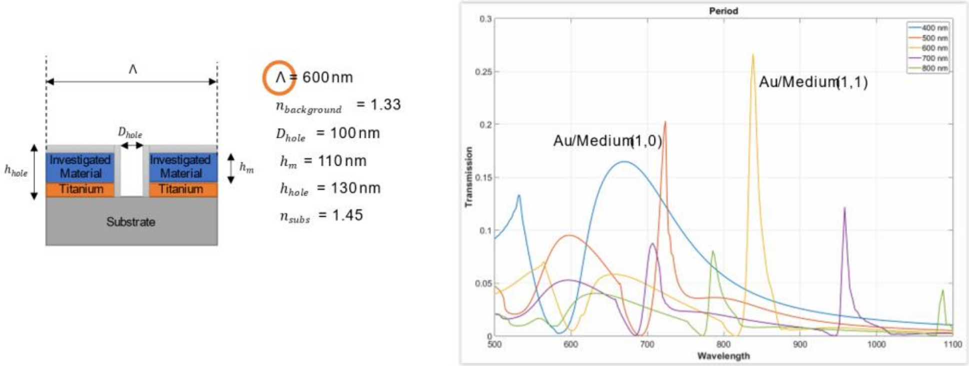

Figure 4.10: Period results for Au. Period values were chosen as 400 nm, 500nm, 600 nm, 700 nm, 800 nm.

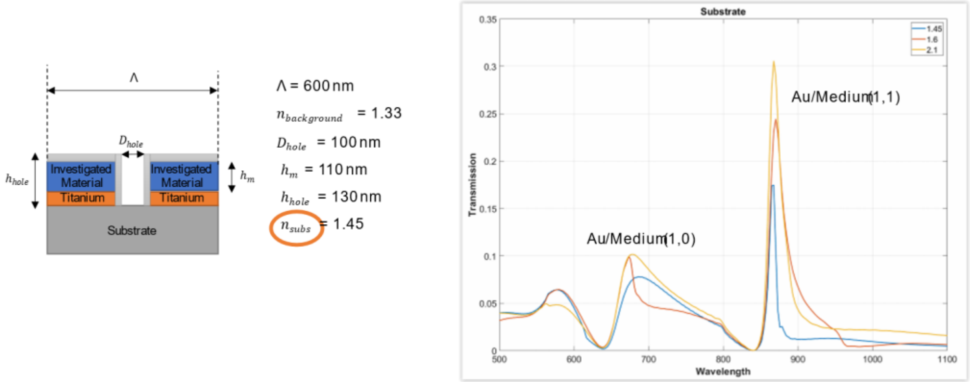

Figure 4.11: Substrate results for Au. Substrate indexes were chosen as 1.45, 1.5, 2.1.

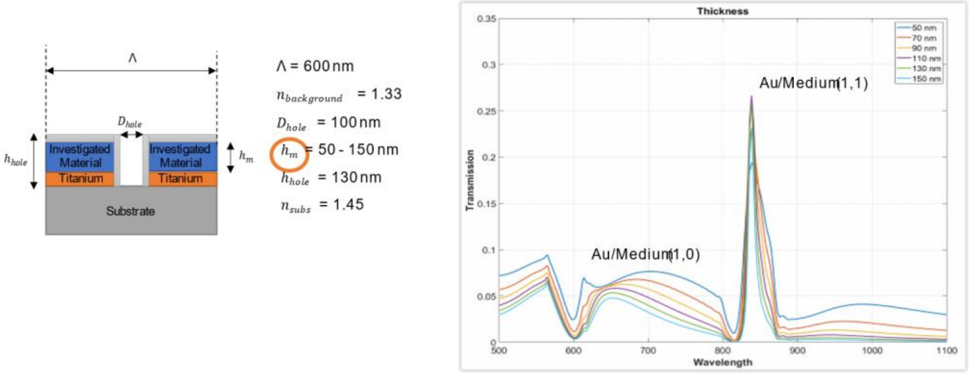

Figure 4.12: Thickness results for Ag. Thickness values were chosen as 50 nm, 70 nm, 90 nm, 110 nm, 130 nm, 150 nm.

4.1.3. Results for aluminum (Al)

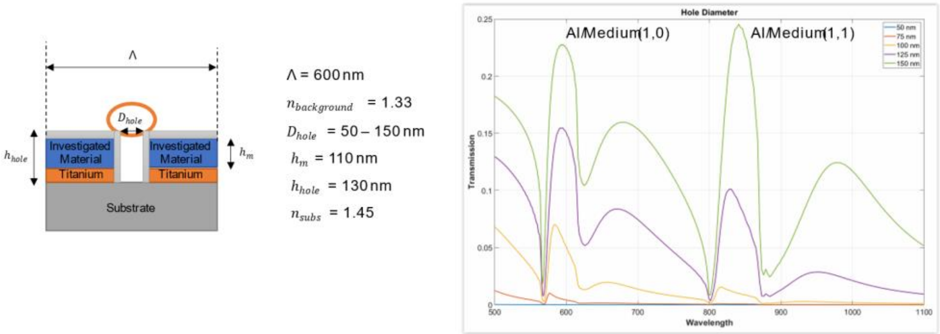

Figure 4.13: Hole diameter simulation results for Al. Diameter values were chosen as 50 nm, 75 nm, 100 nm, 125 nm, 150 nm.

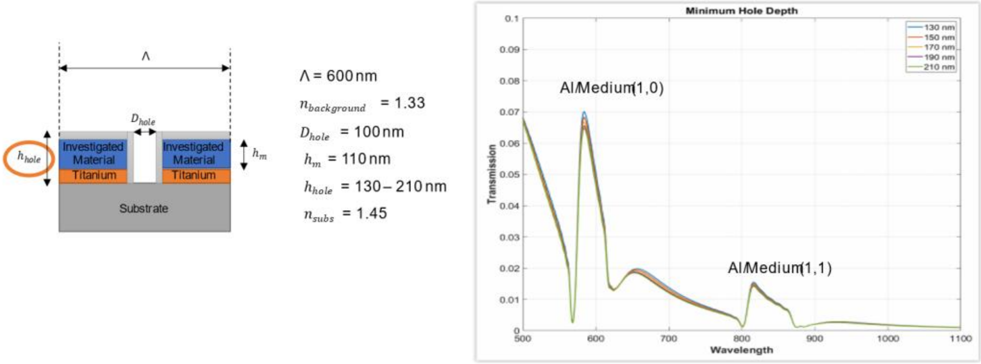

Figure 4.14: Hole depth simulation results for Al. Depth values were chosen as 130 nm, 150 nm, 170 nm, 210 nm.

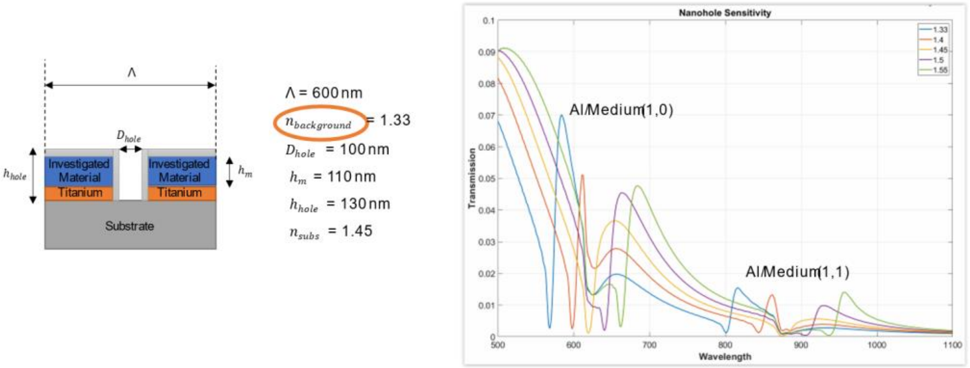

Figure 4.15: Nanohole sensitivity results for Al. Background index values were chosen as 1.33, 1.4, 1.45, 1.5, 1.55.

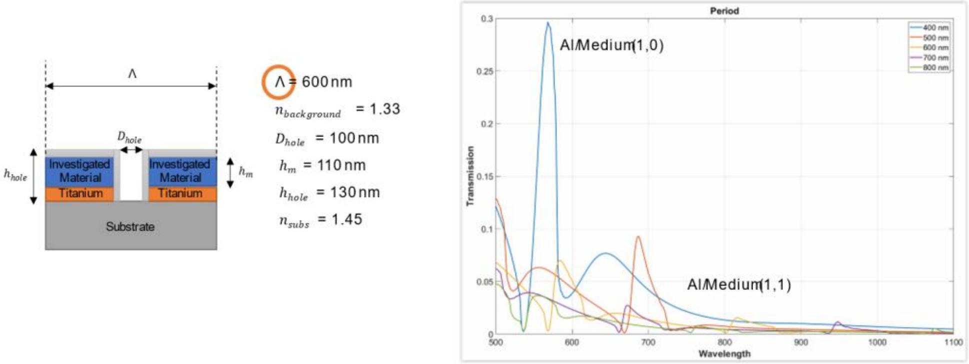

Figure 4.16: Period results for Al. Period values were chosen as 400 nm, 500nm, 600 nm, 700 nm, 800 nm.

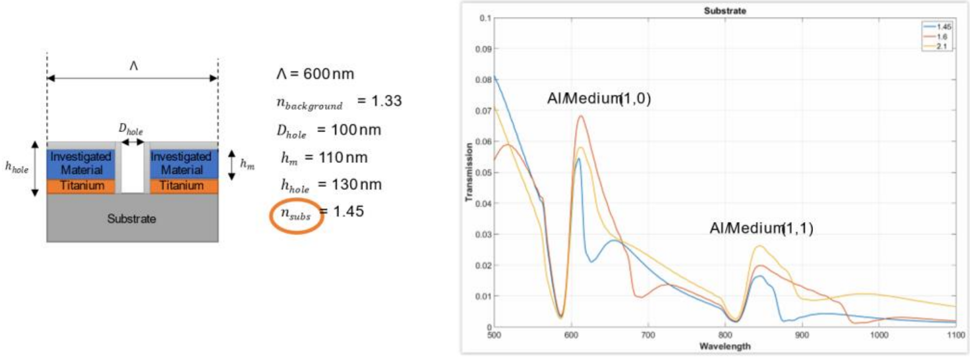

Figure 4.17: Substrate results for Al. Substrate indexes were chosen as 1.45, 1.5, 2.1.

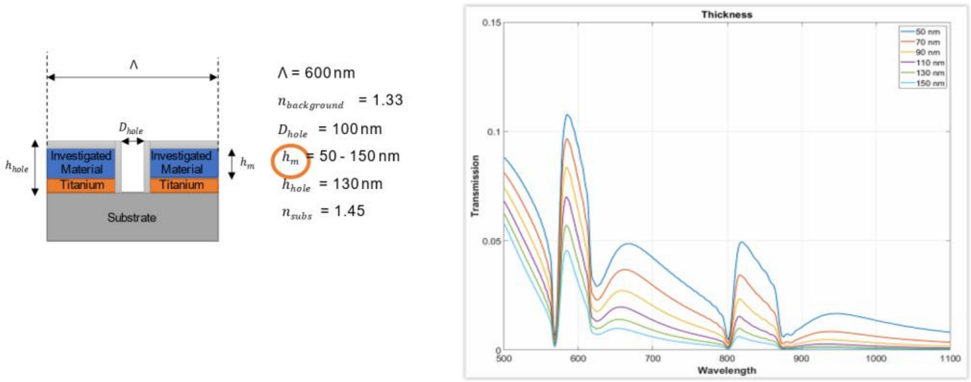

Figure 4.18: Thickness results for Al. Thickness values were chosen as 50 nm, 70 nm, 90 nm, 110 nm, 130 nm, 150 nm.

4.1.4. Results for titanium nitride (TiN)

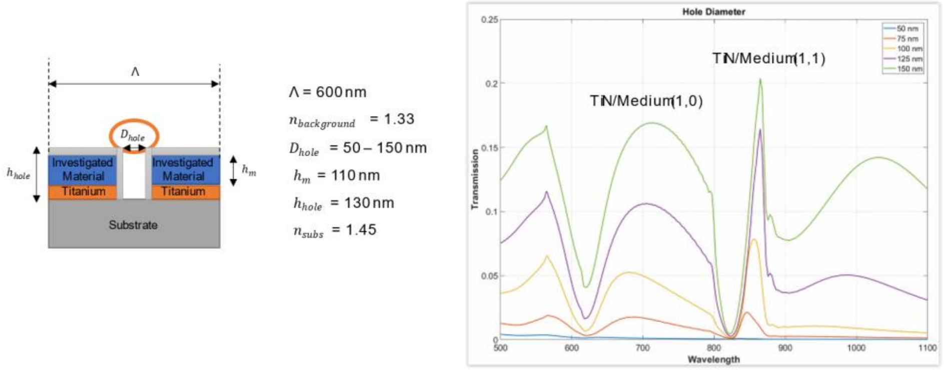

Figure 4.19: Hole diameter simulation results for TiN. Diameter values were chosen as 50 nm, 75 nm, 100 nm, 125 nm, 150 nm.

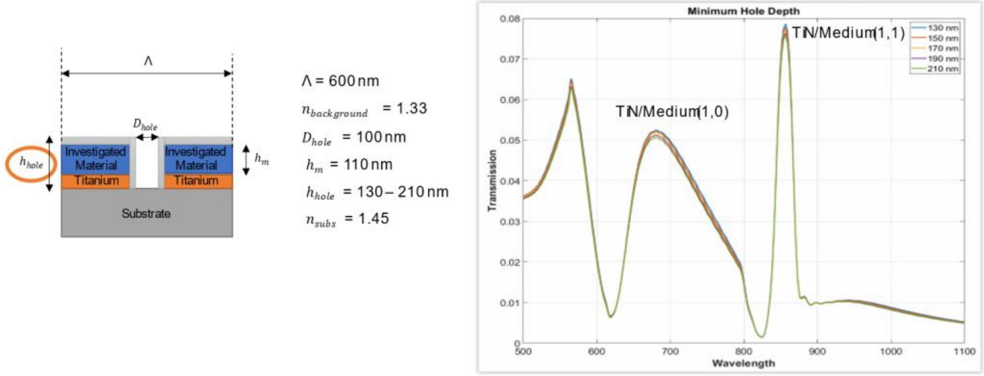

Figure 4.20: Hole depth simulation results for TiN. Depth values were chosen as 130 nm, 150 nm, 170 nm, 210 nm.

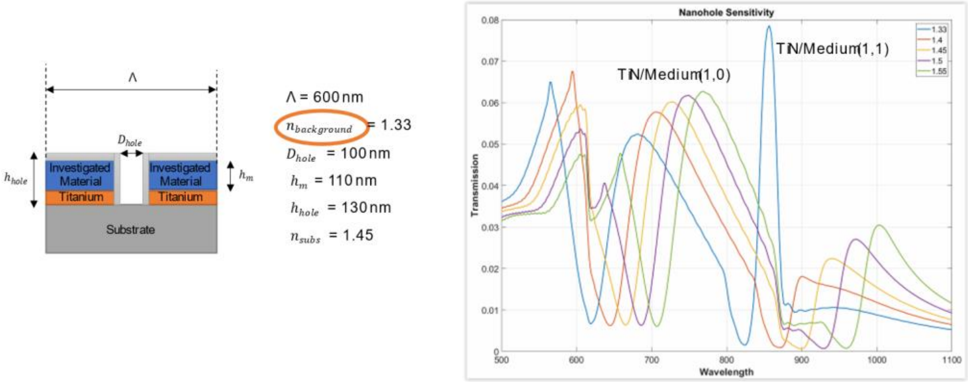

Figure 4.21: Nanohole sensitivity results for TiN. Background index values were chosen as 1.33, 1.4, 1.45, 1.5, 1.55.

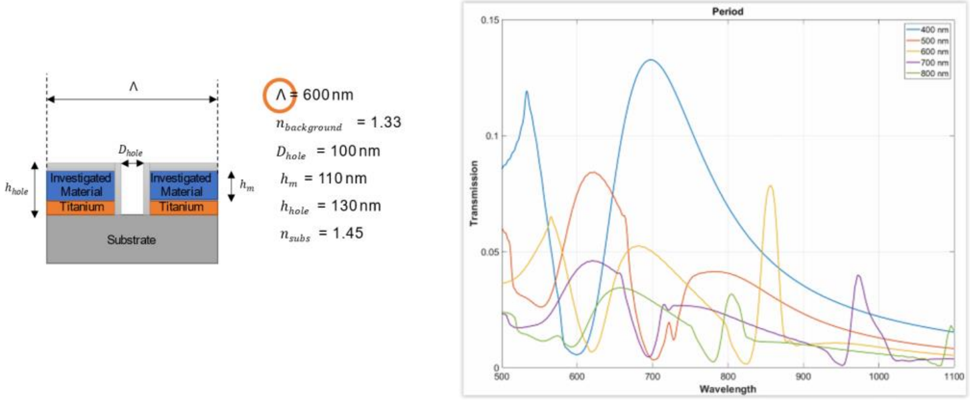

Figure 4.22: Period results for TiN. Period values were chosen as 400 nm, 500nm, 600 nm, 700 nm, 800 nm.

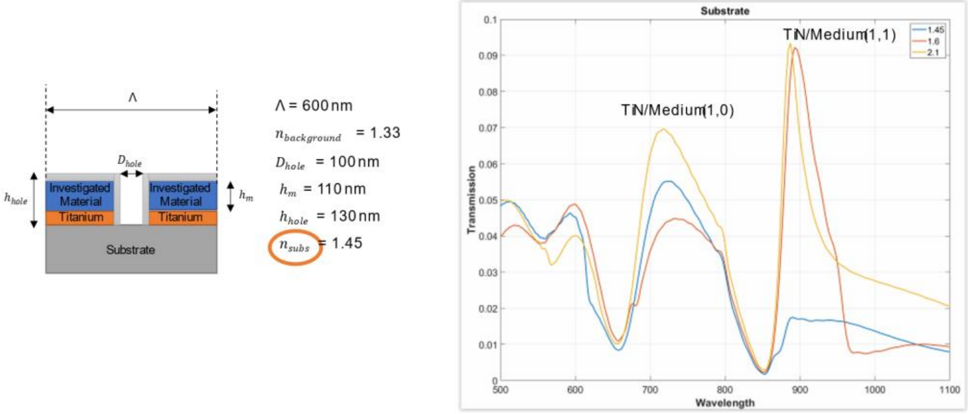

Figure 4.23: Substrate results for TiN. Substrate indexes were chosen as 1.45, 1.5, 2.1.

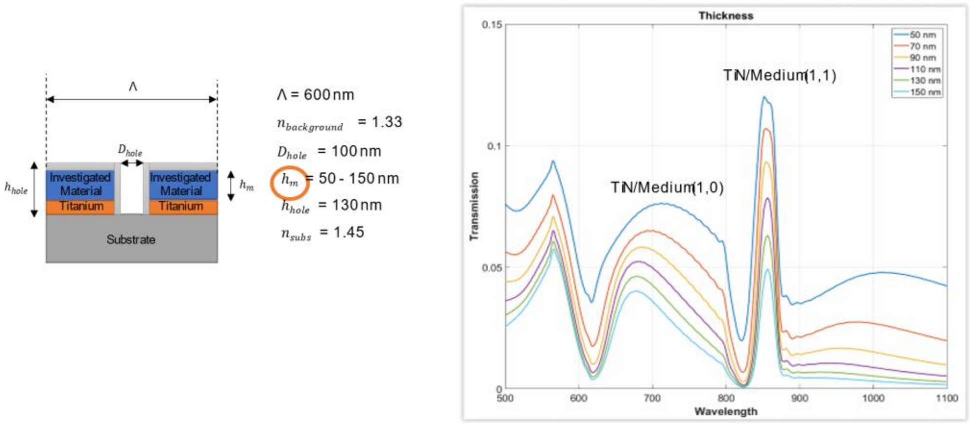

Figure 4.24: Thickness results for TiN. Thickness values were chosen as 50 nm, 70 nm, 90 nm, 110 nm, 130 nm, 150 nm.

4.1.5. Results for titanium nitride (TiN_Guo)

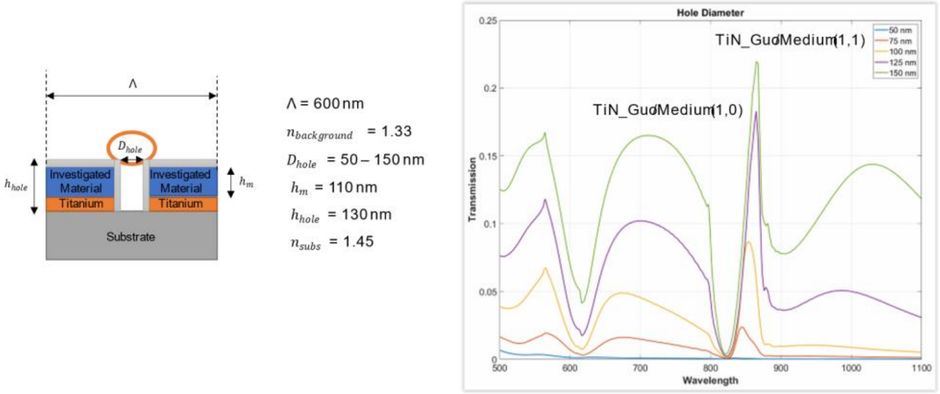

Figure 4.25: Hole diameter simulation results for TiN_Guo. Diameter values were chosen as 50 nm, 75 nm, 100 nm, 125 nm, 150 nm.

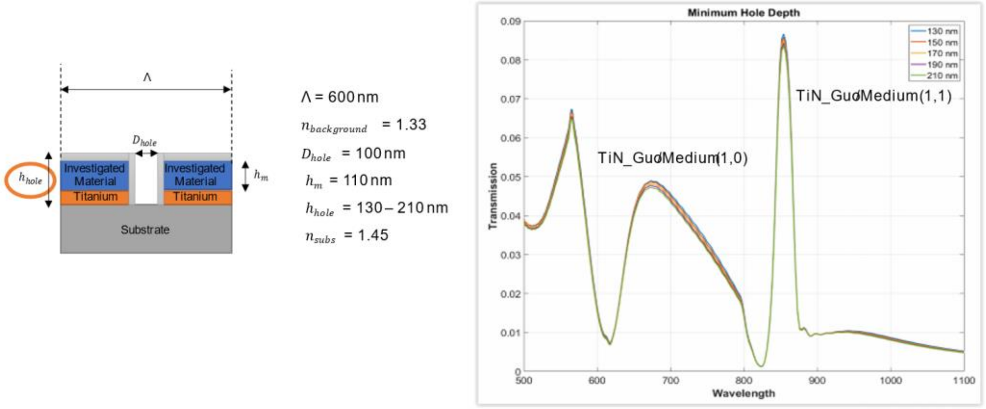

Figure 4.26: Hole depth simulation results for TiN. Depth values were chosen as 130 nm, 150 nm, 170 nm, 210 nm.

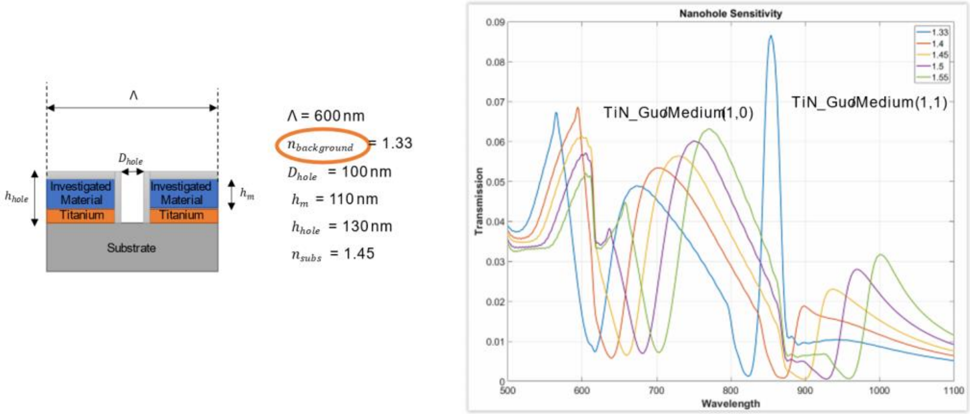

Figure 4.27: Nanohole sensitivity results for TiN. Background index values were chosen as 1.33, 1.4, 1.45, 1.5, 1.55.

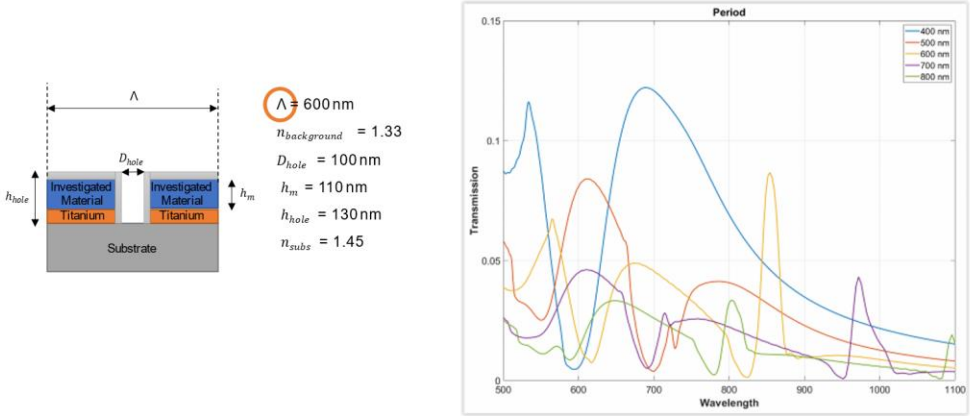

Figure 4.28: Period results for TiN. Period values were chosen as 400 nm, 500nm, 600 nm, 700 nm, 800 nm.

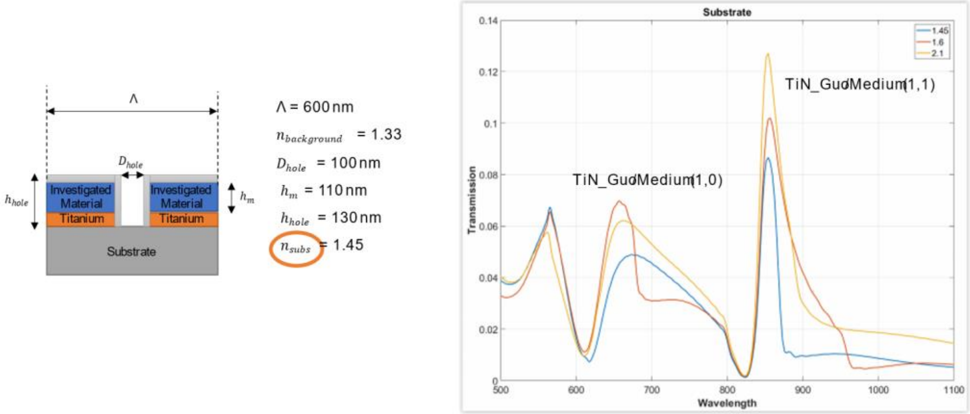

Figure 4.29: Substrate results for TiN. Substrate indexes were chosen as 1.45, 1.5, 2.1.

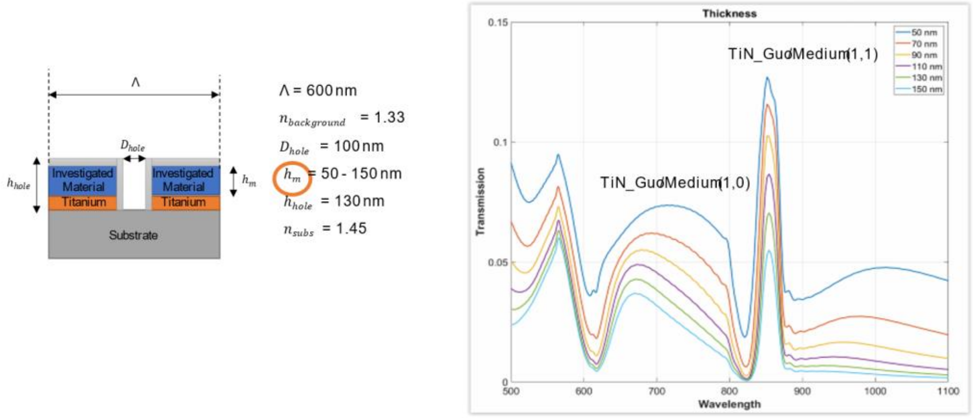

Figure 4.30: Thickness results for TiN. Thickness values were chosen as 50 nm, 70 nm, 90 nm, 110 nm, 130 nm, 150 nm.

4.1.6. Results for hafnium nitride (HfN)

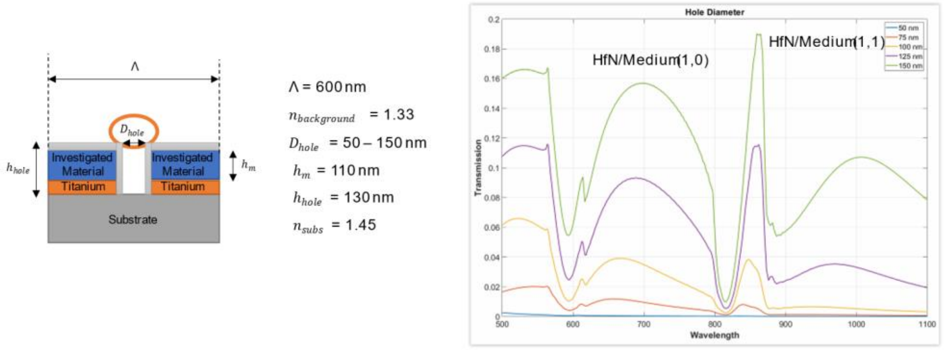

Figure 4.31: Hole diameter simulation results for HfN. Diameter values were chosen as 50 nm, 75 nm, 100 nm, 125 nm, 150 nm.

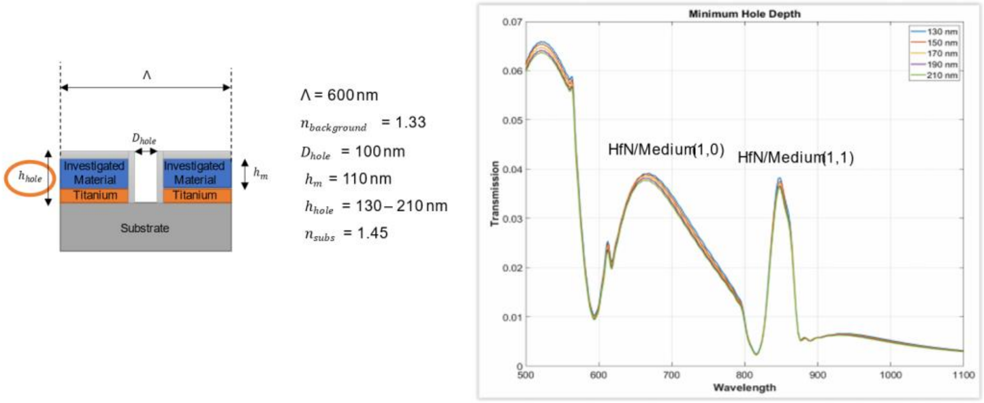

Figure 4.32: Hole depth simulation results for HfN. Depth values were chosen as 130 nm, 150 nm, 170 nm, 210 nm.

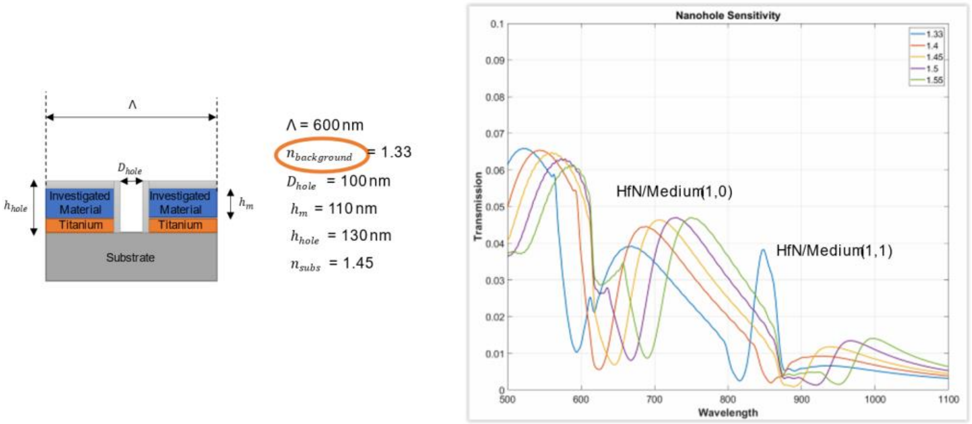

Figure 4.33: Nanohole sensitivity results for HfN. Background index values were chosen as 1.33, 1.4, 1.45, 1.5, 1.55.

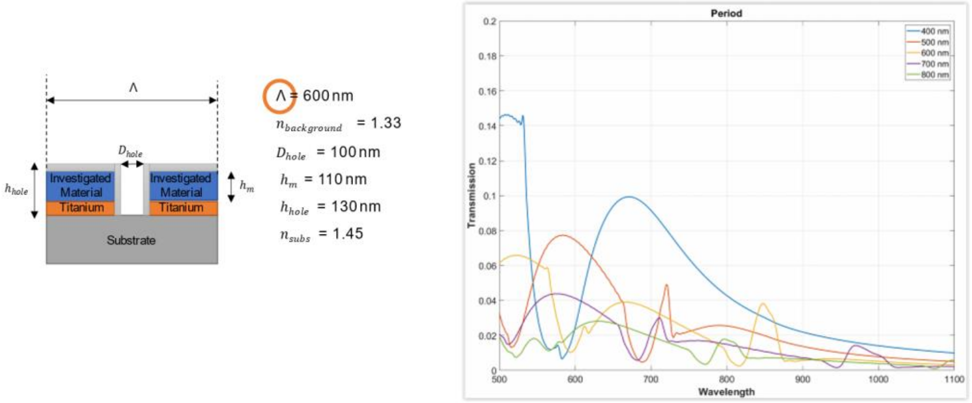

Figure 4.34: Period results for HfN. Period values were chosen as 400 nm, 500nm, 600 nm, 700 nm, 800 nm.

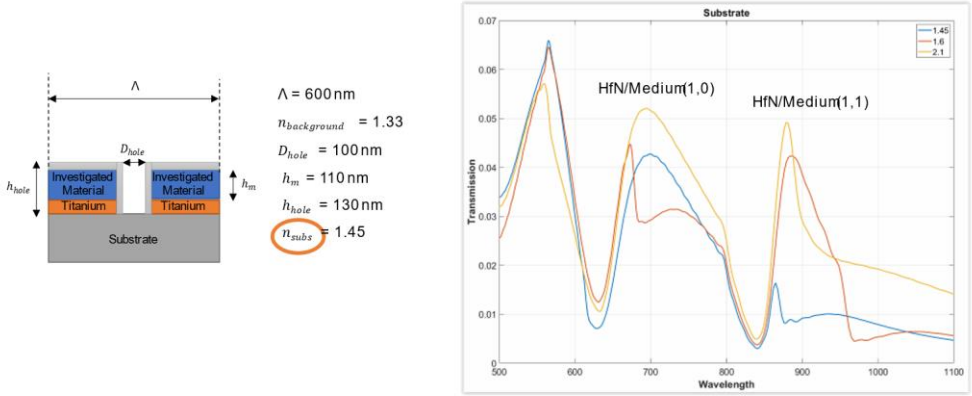

Figure 4.35: Substrate results for HfN. Substrate indexes were chosen as 1.45, 1.5, 2.1.

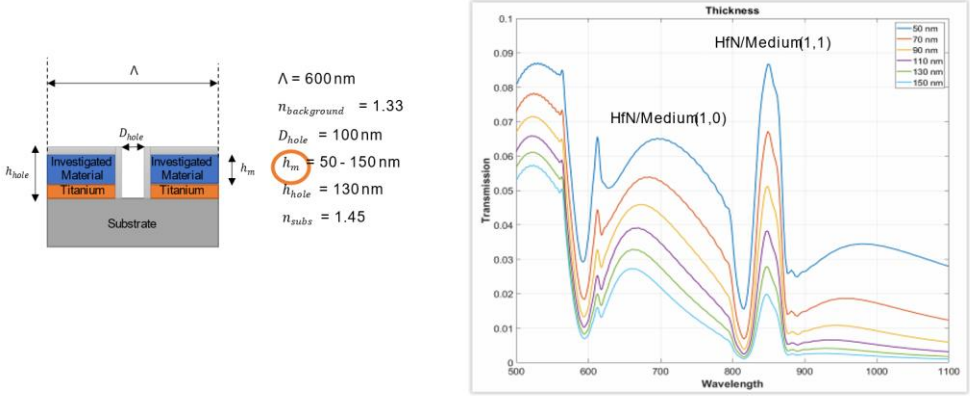

Figure 4.36: Thickness results for HfN. Thickness values were chosen as 50 nm, 70 nm, 90 nm, 110 nm, 130 nm, 150 nm.

4.1.7. Results for zirconium nitride (ZrN_Guler)

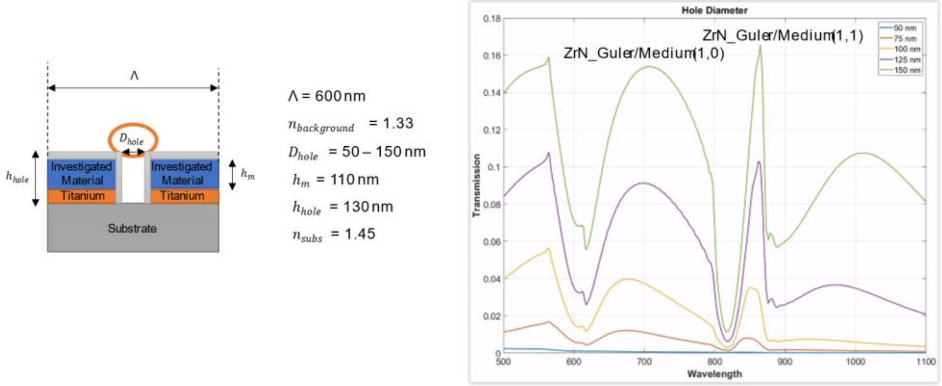

Figure 4.37: Hole diameter simulation results for ZrN_Guler. Diameter values were chosen as 50 nm, 75 nm, 100 nm, 125 nm, 150 nm.

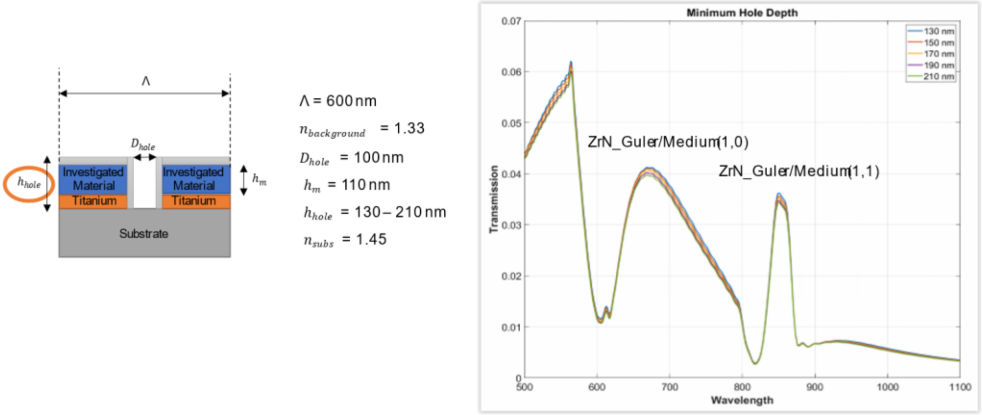

Figure 4.38: Hole depth simulation results for ZrN_Guler. Depth values were chosen as 130 nm, 150 nm, 170 nm, 210 nm.

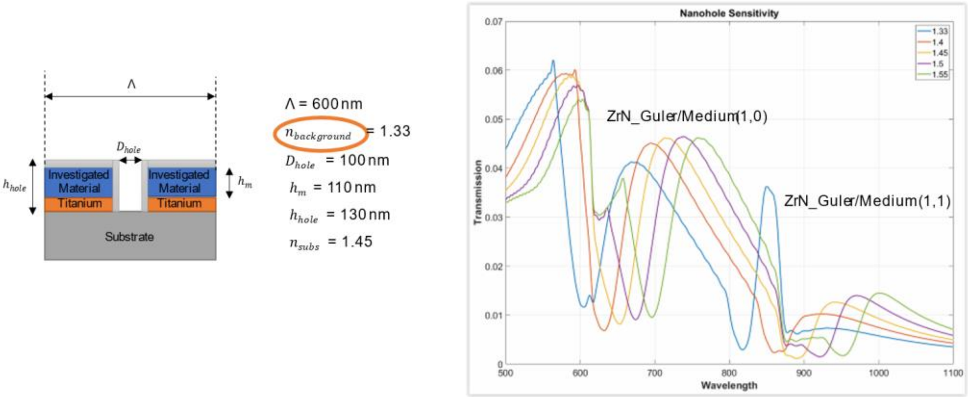

Figure 4.39: Nanohole sensitivity results for ZrN_Guler. Background index values were chosen as 1.33, 1.4, 1.45, 1.5, 1.55.

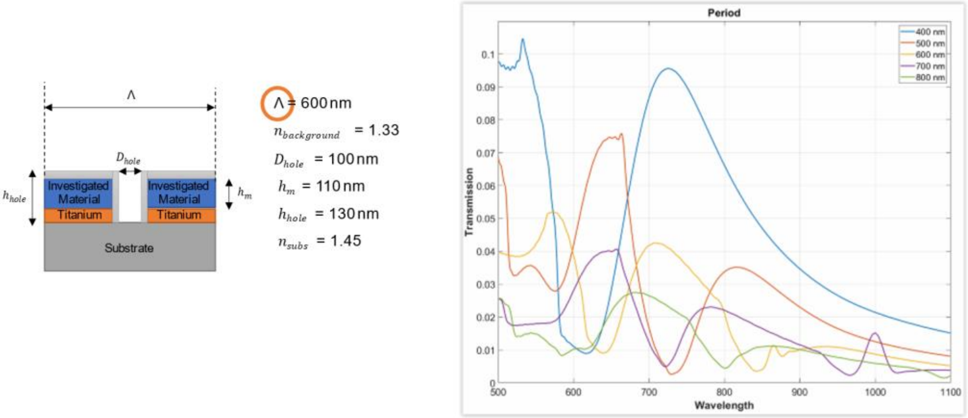

Figure 4.40: Period results for ZrN_Guler. Period values were chosen as 400 nm, 500nm, 600 nm, 700 nm, 800 nm.

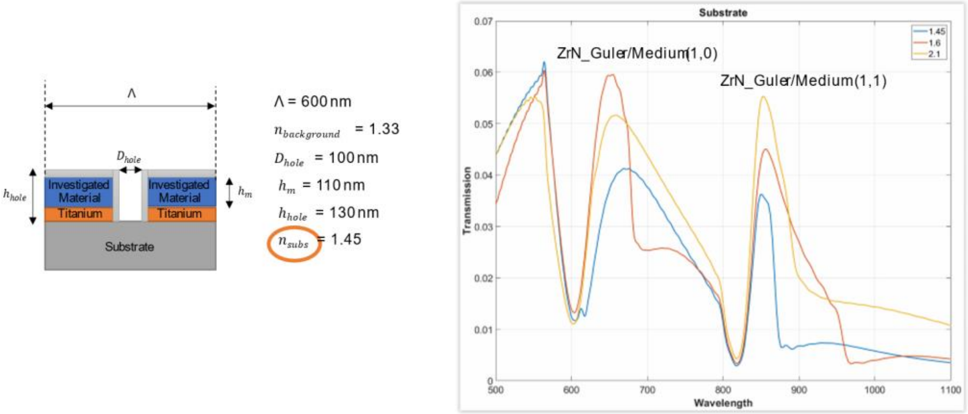

Figure 4.41: Substrate results for ZrN_Guler. Substrate indexes were chosen as 1.45, 1.5, 2.1.

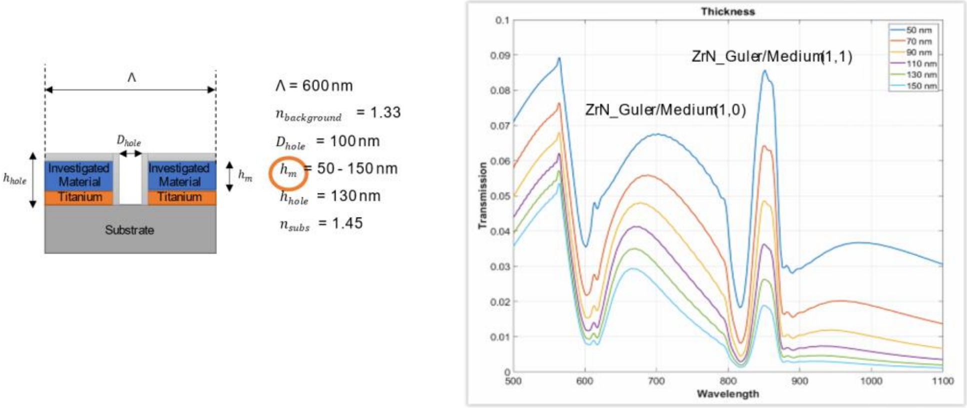

Figure 4.42: Thickness results for ZrN_Guler. Thickness values were chosen as 50 nm, 70 nm, 90 nm, 110 nm, 130 nm, 150 nm.

4.1.8. Results for zirconium nitride (ZrN_Naik)

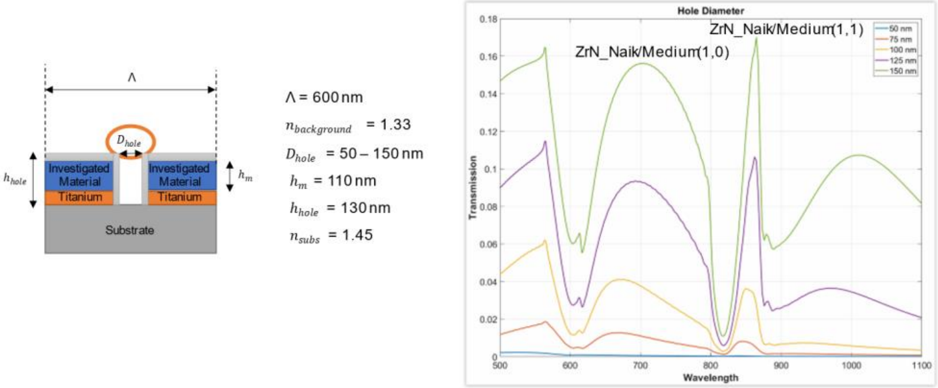

Figure 4.43: Hole diameter simulation results for ZrN_Guler. Diameter values were chosen as 50 nm, 75 nm, 100 nm, 125 nm, 150 nm.

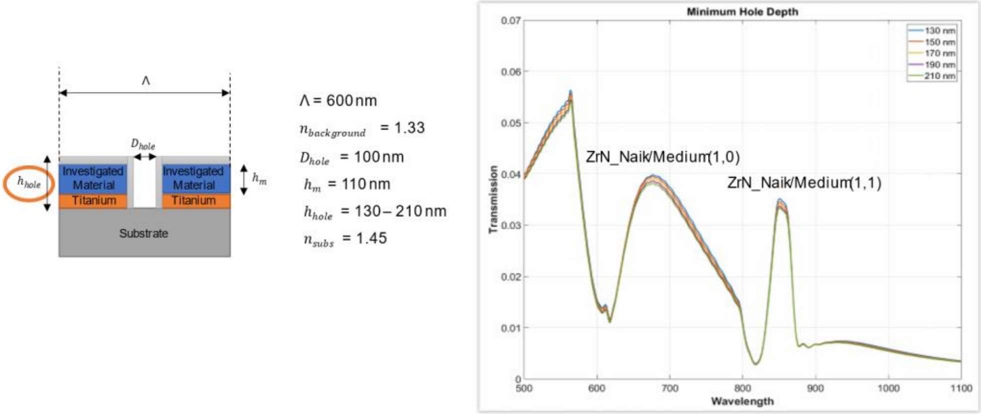

Figure 4.44: Hole depth simulation results for ZrN_Guler. Depth values were chosen as 130 nm, 150 nm, 170 nm, 210 nm.

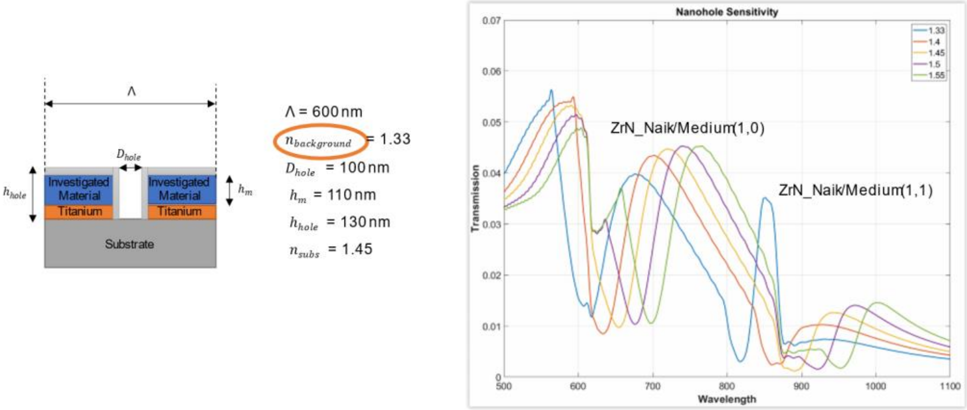

Figure 4.45: Nanohole sensitivity results for ZrN_Guler. Background index values were chosen as 1.33, 1.4, 1.45, 1.5, 1.55.

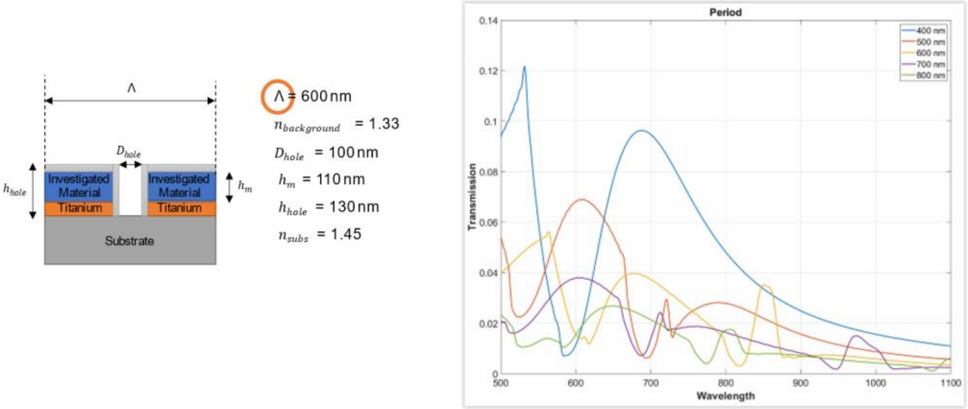

Figure 4.46: Period results for ZrN_Guler. Period values were chosen as 400 nm, 500nm, 600 nm, 700 nm, 800 nm.

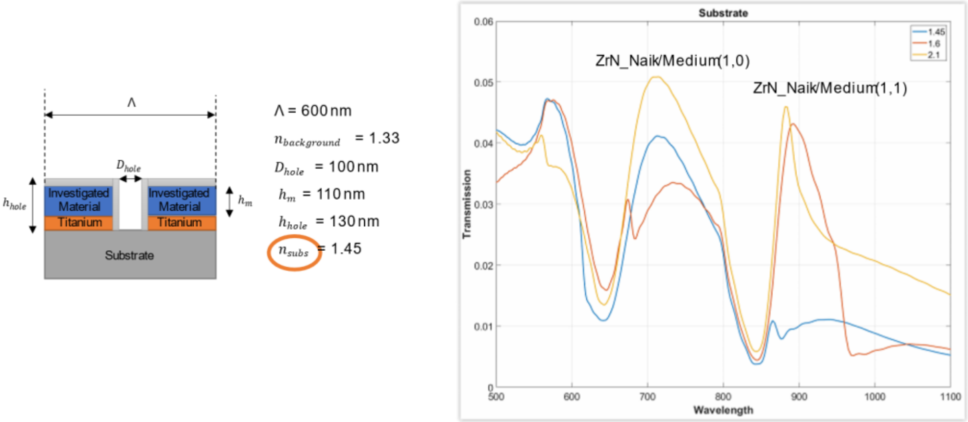

Figure 4.47: Substrate results for ZrN_Guler. Substrate indexes were chosen as 1.45, 1.5, 2.1.

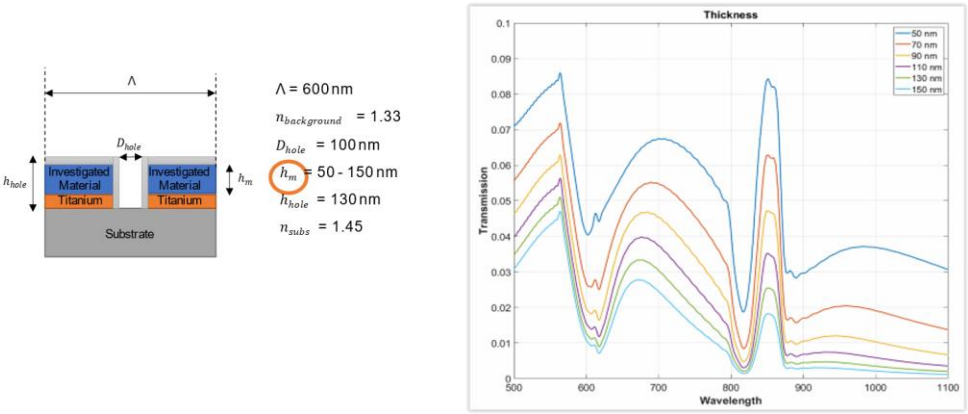

Figure 4.48: Thickness results for ZrN_Guler. Thickness values were chosen as 50 nm, 70 nm, 90 nm, 110 nm, 130 nm, 150 nm.

4.2. SLR Results

4.2.1. Results for gold (Au)

4.2.1.1. Nanohole diameter 100 nm

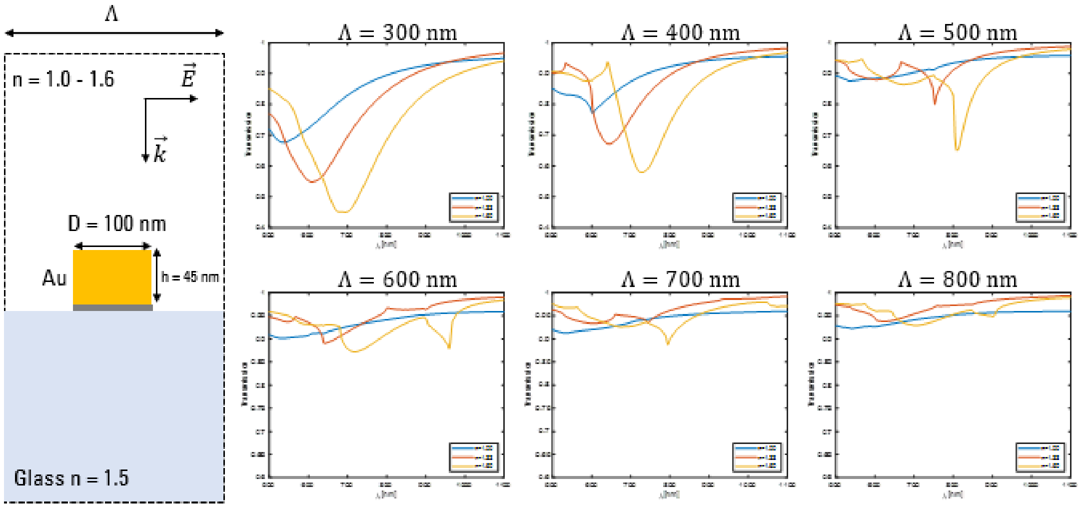

Figure 4.49: 100 nm diameter results for Au nanodisc.

4.2.1.2. Nanohole diameter 150 nm

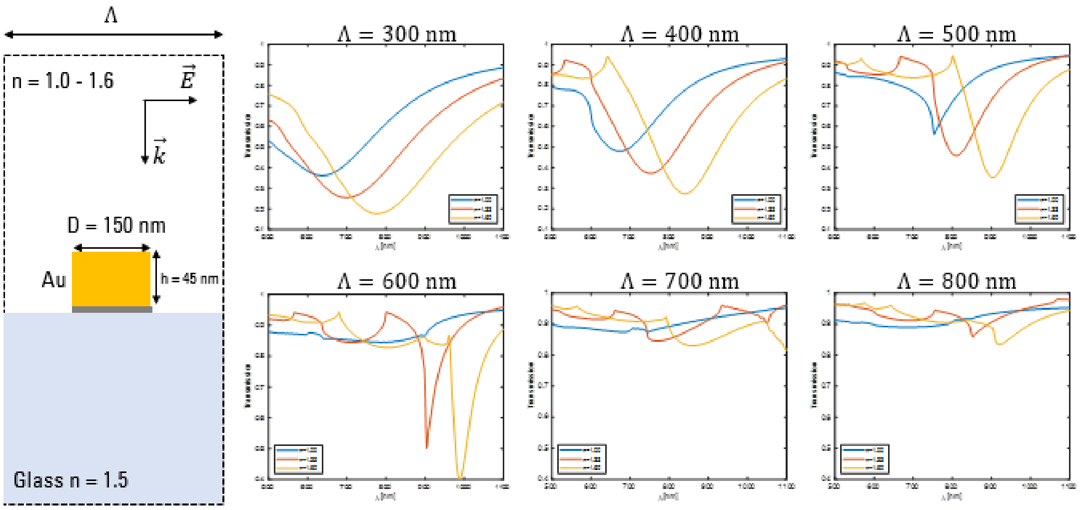

Figure 4.50: 150 nm diameter results for Au nanodisc.

4.2.1.3. Nanohole diameter 200 nm

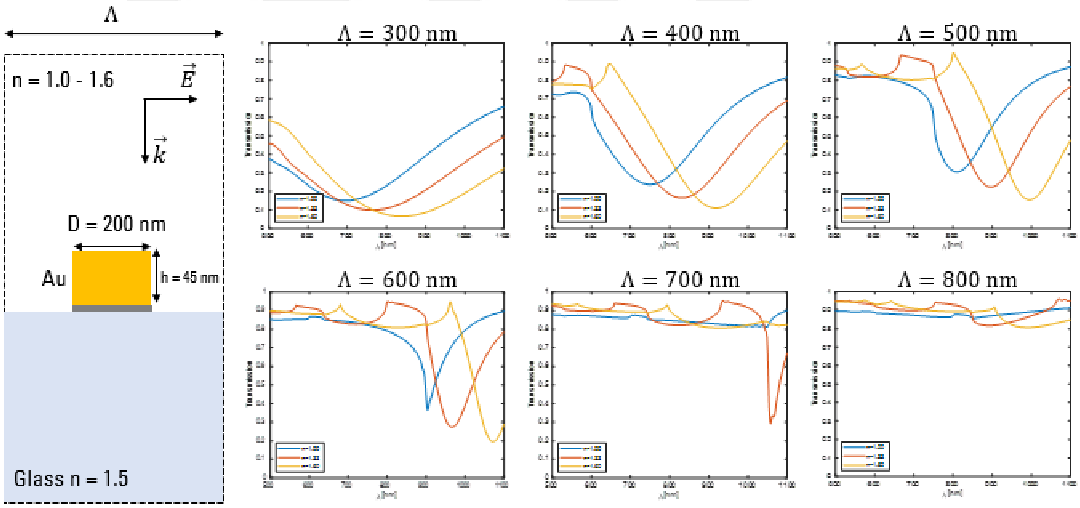

Figure 4.51: 200 nm diameter results for Au nanodisc.

4.2.1.4. Nanohole diameter 250 nm

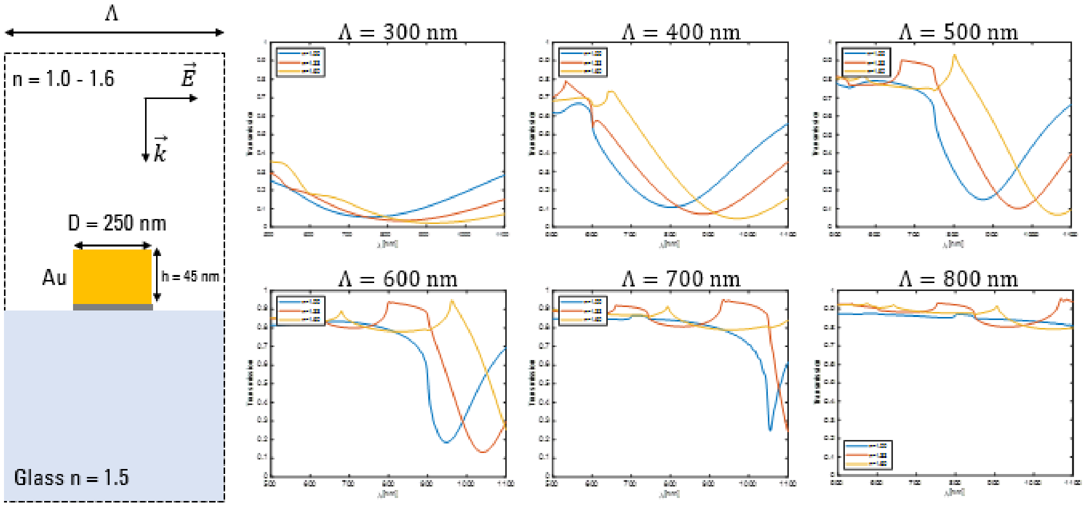

Figure 4.52: 250 nm diameter results for Au nanodisc.

4.2.2. Results for titanium nitride (TiN)

4.2.2.1. Nanohole diameter for 100 nm

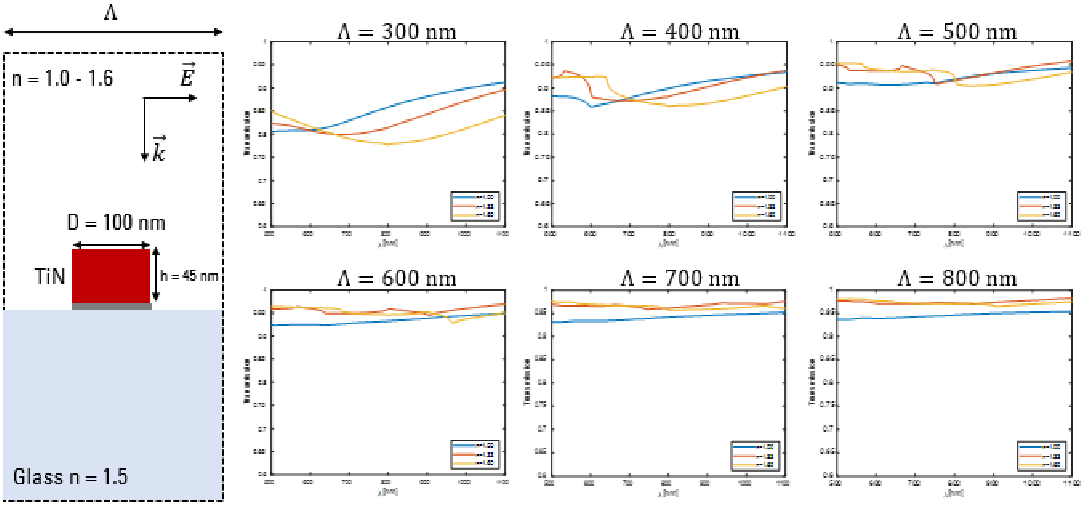

Figure 4.53: 100 nm diameter results for TiN nanodisc.

4.2.2.2. Nanohole diameter for 150 nm

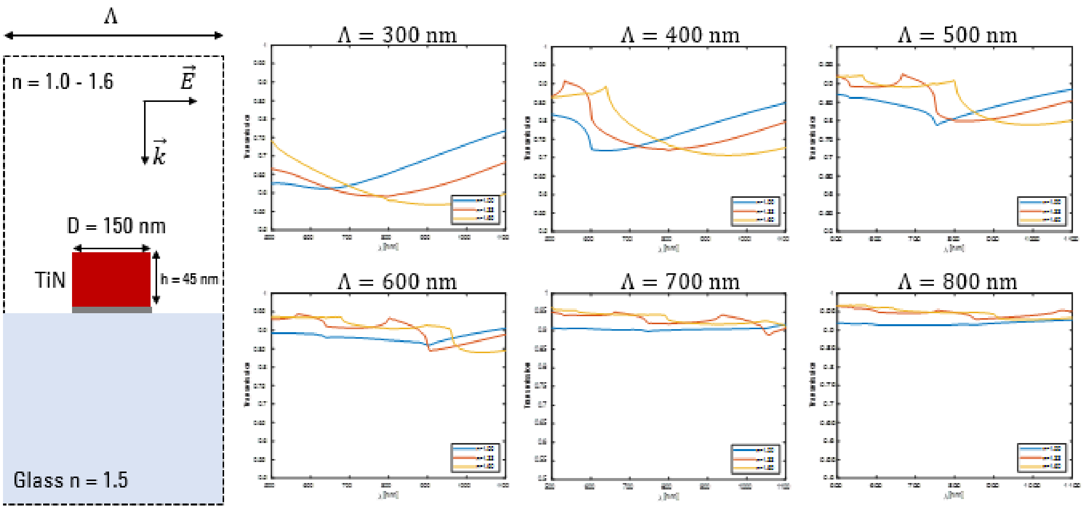

Figure 4.54: 150 nm diameter results for TiN nanodisc.

4.2.2.3. Nanohole diameter 200 nm

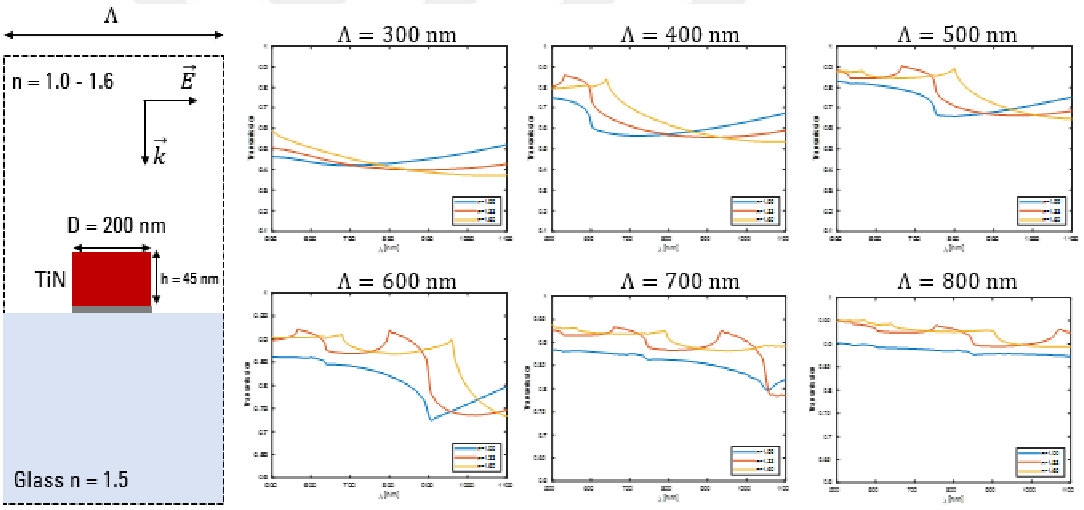

Figure 4.55: 200 nm diameter results for TiN nanodisc.

4.2.2.4. Nanohole diameter 250 nm

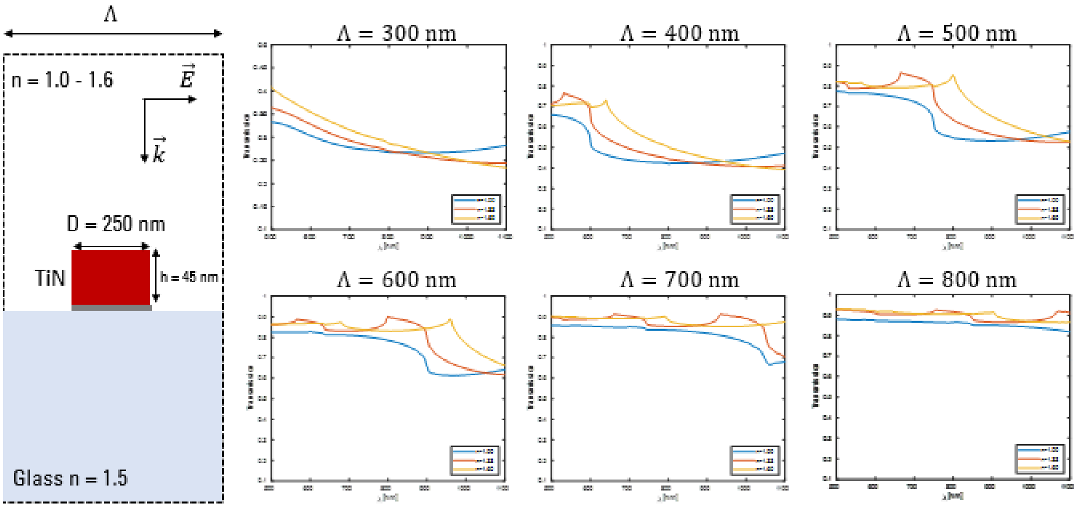

Figure 4.56: 250 nm diameter results for TiN nanodisc.

4.2.3. Results for hafnium nitride (HfN)

4.2.3.1. Nanohole diameter 100 nm

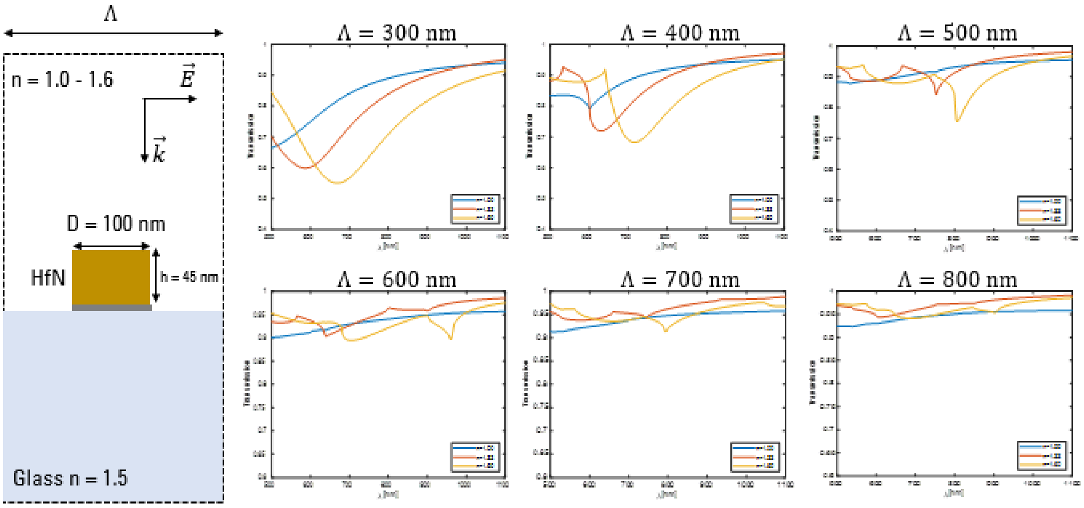

Figure 4.57: 100 nm diameter results for HfN nanodisc.

4.2.3.2. Nanohole diameter 150 nm

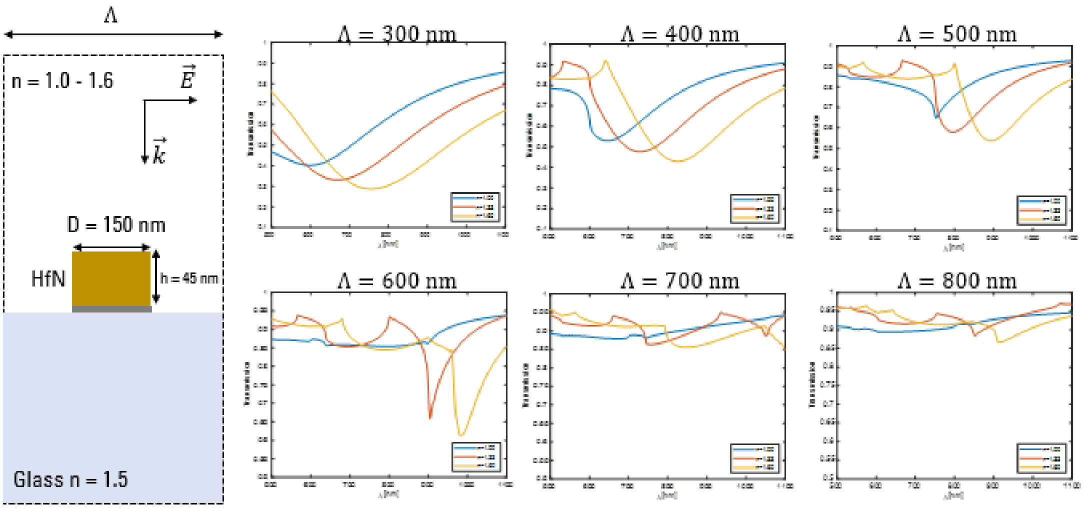

Figure 4.58: 150 nm diameter results for HfN nanodisc.

4.2.3.3. Nanohole diameter 200 nm

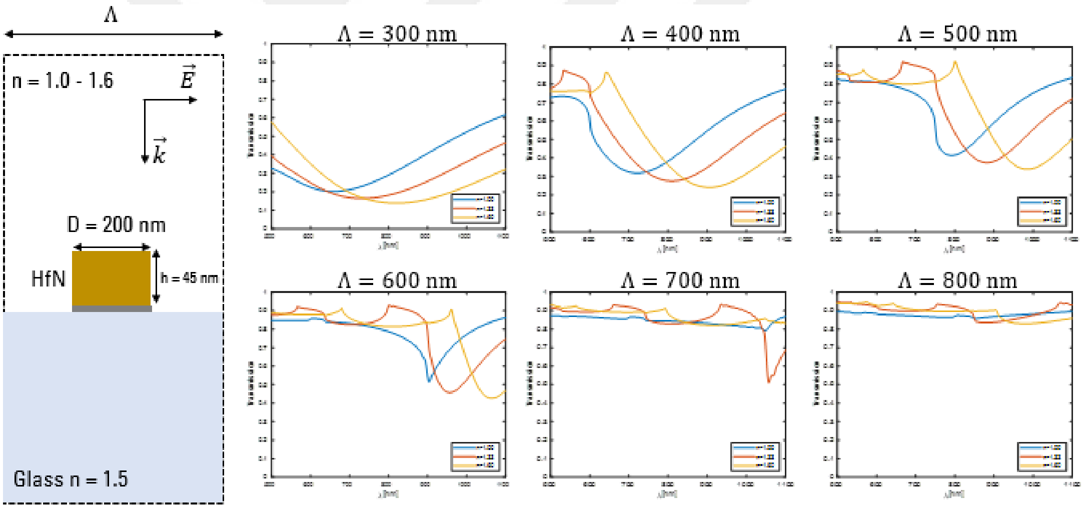

Figure 4.59: 200 nm diameter results for HfN nanodisc.

4.2.3.4. Nanohole diameter 250 nm

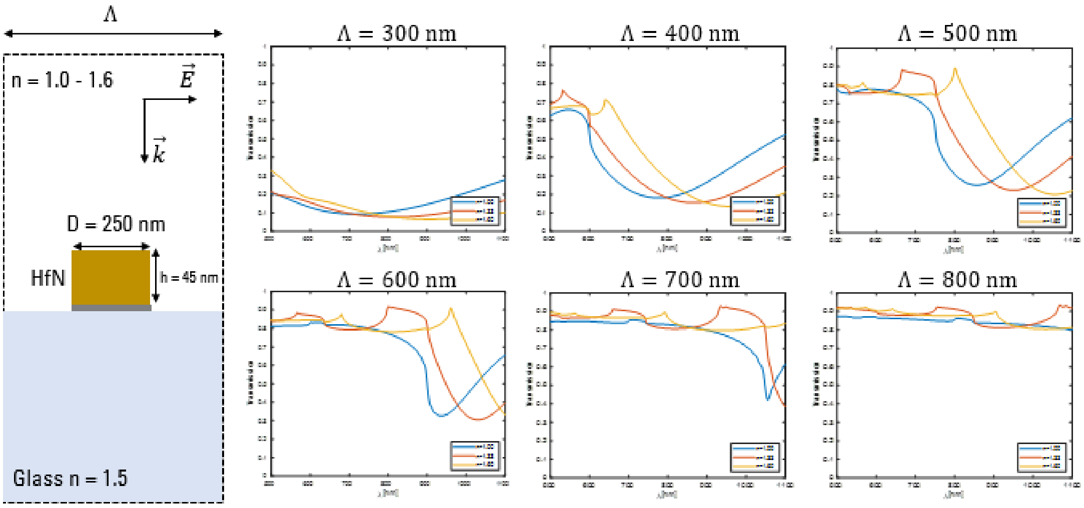

Figure 4.60: 250 nm diameter results for HfN nanodisc.

4.2.4. Results for zirconium nitride (ZrN)

4.2.4.1. Nanohole diameter 100 nm

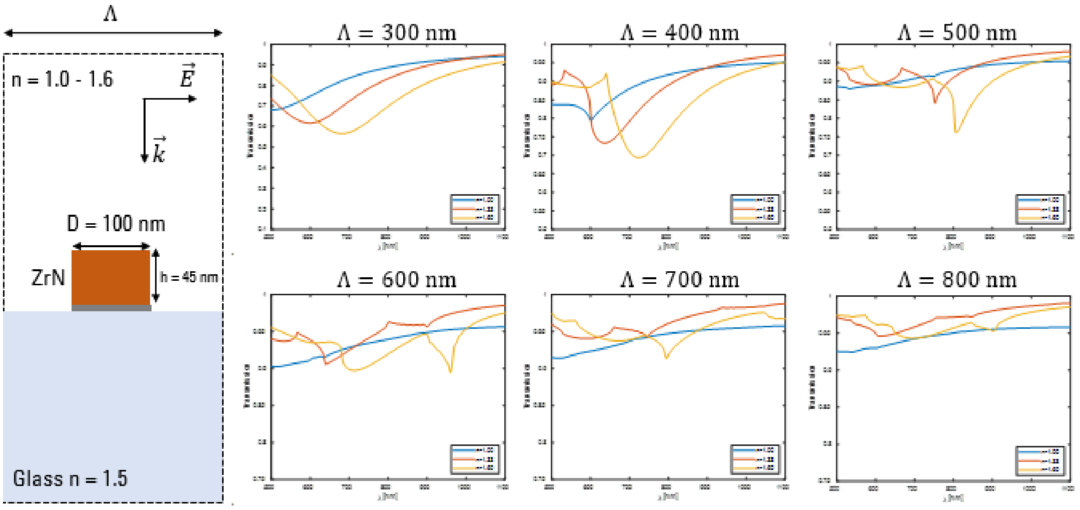

Figure 4.61: 100 nm diameter results for ZrN nanodisc.

4.2.4.2. Nanohole diameter 150 nm

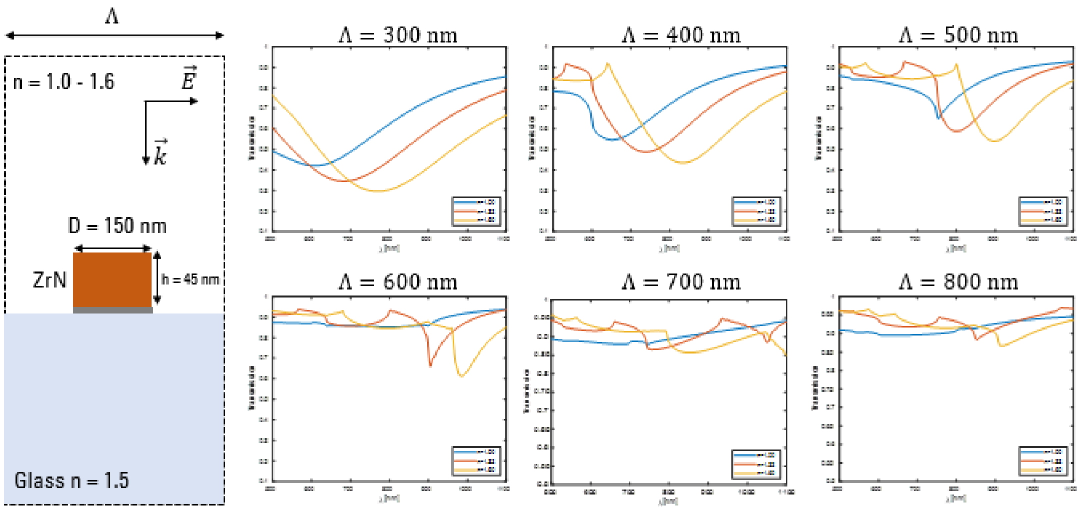

Figure 4.62: 150 nm diameter results for ZrN nanodisc.

4.2.4.3. Nanohole diameter 200 nm

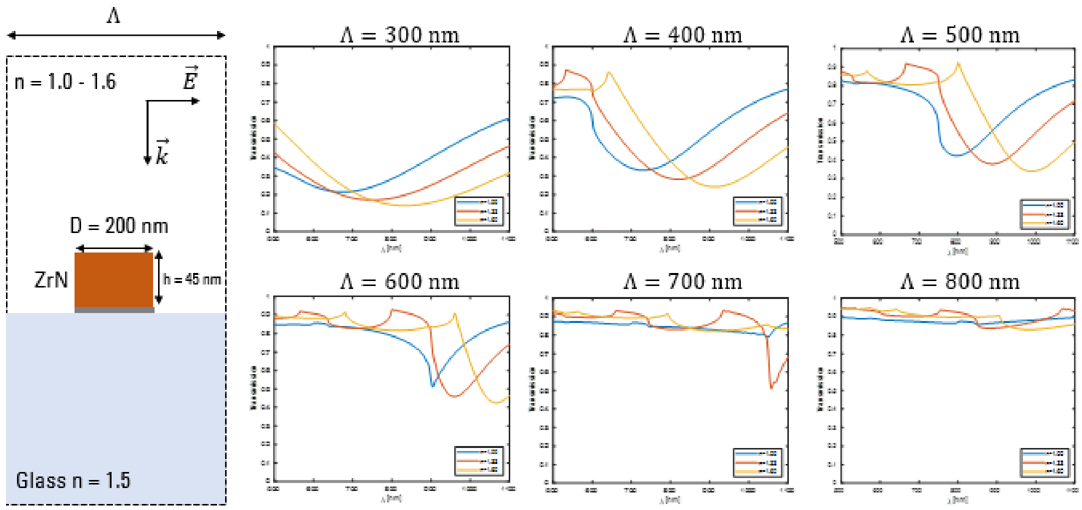

Figure 4.63: 200 nm diameter results for ZrN nanodisc.

4.2.4.4. Nanohole diameter 250 nm

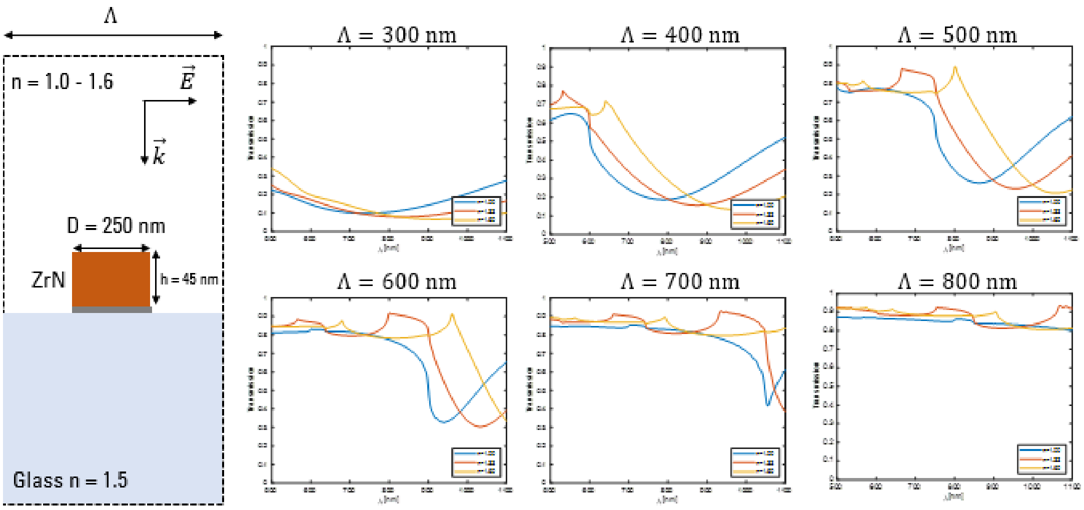

Figure 4.64: 250 nm diameter results for ZrN nanodisc.

CHAPTER 5

5. CONCLUSIONS AND FUTURE WORK

Plasmonic keep developing and getting a big industry in electro-optical applications. Discovery of new methods makes it more useful for manipulation of light. It became very important for healthcare applications due to its use in biosensors. The pandemic that whole world is facing since 2019 cause nanotechnology researches to increase more rapidly than ever. Market value of the biosensors expected to increase from 25.5 million USD to 36.7 million USD in 5 years from 2021 to 2026. Popularity of gold and silver started to diminish due to their high costs, nanofabrication challenges etc. for this endless variety of different application of plasmonic. New alternative materials like aluminum, copper and metal nitrides started to be investigated for light manipulation instead of gold and silver. In this thesis, these alternative materials are investigated with two configuration which are nanohole array and nanodisc in terms of their ability to manipulate light according to their nanohole periods, nanohole radius, material thickness and nanohole sensitivity.

SPR simulations were prepared and implemented in Lumerical software. Nanoholes are designed and parameters were chosen as decided. Silver followed by gold demonstrated the best performance as expected. Among the alternative materials aluminum's full width half maxima values were very large than optimal. For zirconium nitride and hafnium nitride, their peak values were too low compared to the other materials. On the other hand, eventhough titanium nitrides peak values were not high as much as gold and silver, its full width half maxima were in acceptable range. Especially, between 800 nm and 900 nm titanium nitride performance in a nanohole configuration is promising. This result demonstrated titanium nitride can be a candidate for nanohole plasmonic applications between 800 nm and 900 nm.

Another configuration that conducted in this thesis was nanodisc configuration. Nanodiscs are prepared and parameters were altered as decided in the experimental part. In this configuration only one titanium nitride and zirconium nitride were utilized due to results were almost identical. Titanium nitride demonstrated poor performance eventhough its good results in nanoholes. Another nitride’s which is hafnium nitride was better than the titanium nitride and zirconium nitride. Especially for the 150 nm diameter with 600 nm periodicity its results are promising. It has a good peak value and acceptable full width half maxima.

As a result, domination of gold and silver is till strong in plasmonic field however, researches like this thesis demonstrates some alternative materials can be used instead of gold and silver for specific application. Performance amplification studies can improve performance of these alternative materials and may be one day a material such as titanium nitride or hafnium nitride can overcome dominion of gold and silver. Detailed study done for this thesis may inspire other studies and researches to achieve this aim.

BIBLIOGRAPHY

[1] I. Pérez-Juste and O. N. Faza, “Interaction of Radiation with Matter,” 2015.

[2] A. M. Shrivastav, U. Cvelbar, and I. Abdulhalim, “A comprehensive review on plasmonic-based biosensors used in viral diagnostics,” *Communications Biology*, vol. 4, no. 1. Nature Research, Dec. 01, 2021. doi: 10.1038/s42003-020-01615-8.

[3] G. v. Naik, V. M. Shalaev, and A. Boltasseva, “Alternative plasmonic materials: Beyond gold and silver,” *Advanced Materials*, vol. 25, no. 24. pp. 3264–3294, Jun. 25, 2013. doi: 10.1002/adma.201205076.

[4] Maier S. A. “Plasmonics: fundamentals and applications.” *Springer*, 2007 https://doi.org/10.1007/0-387-37825-1

[5] E. Petryayeva and U. J. Krull, “Localized surface plasmon resonance: Nanostructures, bioassays and biosensing-A review,” *Analytica Chimica Acta*, vol. 706, no. 1. pp. 8–24, Nov. 07, 2011. doi: 10.1016/j.aca.2011.08.020.

[6] S. Hayashi and T. Okamoto, “Plasmonics: Visit the past to know the future,” *Journal of Physics D: Applied Physics*, vol. 45, no. 43. Oct. 31, 2012. doi: 10.1088/0022-3727/45/43/433001.

[7] S. Scarano, M. Mascini, A. P. F. Turner, and M. Minunni, “Surface plasmon resonance imaging for affinity-based biosensors,” *Biosensors and Bioelectronics*, vol. 25, no. 5. pp. 957–966, Jan. 15, 2010. doi: 10.1016/j.bios.2009.08.039.

[8] S. Lbfh, M. Malmqvist, I. Rgnnberg, E. Stenberg, B. Liedberg, and I. Lundstrgm, “Bioanalysis with surface plasmon resonance,” 1991.

[9] A. Prasad, J. Choi, Z. Jia, S. Park, and M. R. Gartia, “Nanohole array plasmonic biosensors: Emerging point-of-care applications,” *Biosensors and Bioelectronics*, vol. 130. Elsevier Ltd, pp. 185–203, Apr. 01, 2019. doi: 10.1016/j.bios.2019.01.037.

[10] E. Kazuma and T. Tatsuma, “Localized surface plasmon resonance sensors based on wavelength-tunable spectral dips,” *Nanoscale*, vol. 6, no. 4, pp. 2397–2405, Feb. 2014, doi: 10.1039/c3nr05846h.

[11] Y. Hong, Y. M. Huh, D. S. Yoon, and J. Yang, “Nanobiosensors based on localized surface plasmon resonance for biomarker detection,” *Journal of Nanomaterials*, vol. 2012. 2012. doi: 10.1155/2012/759830.

[12] R. Gordon, D. Sinton, K. L. Kavanagh, and A. G. Brolo, “A new generation of sensors based on extraordinary optical transmission,” *Acc Chem Res*, vol. 41, no. 8, pp. 1049–1057, Aug. 2008, doi: 10.1021/ar800074d.

[13] H. Kurt *et al.*, “Nanoplasmonic biosensors: Theory, structure, design, and review of recent applications,” *Analytica Chimica Acta*. Elsevier B.V., 2021. doi: 10.1016/j.aca.2021.338842.

[14] F. B. P. Niesler, S. Linden, J. Förstner, Y. Grynko, T. Meier, and M. Wegener, “Collective effects in second-harmonic generation from split-ring-resonator arrays,” 2012.

[15] H. Liang, H. Wei, D. Pan, and H. Xu, “Chemically synthesized noble metal nanostructures for plasmonics,” *Nanotechnol Rev*, vol. 4, no. 3, pp. 289–302, Jun. 2015, doi: 10.1515/ntrev-2014-0026.

[16] V. Amendola, R. Pilot, M. Frasconi, O. M. Maragò, and M. A. Iatì, “Surface plasmon resonance in gold nanoparticles: A review,” *Journal of Physics Condensed Matter*, vol. 29, no. 20. Institute of Physics Publishing, Apr. 20, 2017. doi: 10.1088/1361-648X/aa60f3.

[17] A. N. Koya *et al.*, “Nanoporous Metals: From Plasmonic Properties to Applications in Enhanced Spectroscopy and Photocatalysis,” *ACS Nano*, vol. 15, no. 4. American Chemical Society, pp. 6038–6060, Apr. 27, 2021. doi: 10.1021/acsnano.0c10945.

[18] A. Lalisse, G. Tessier, J. Plain, and G. Baffou, “Plasmonic efficiencies of nanoparticles made of metal nitrides (TiN, ZrN) compared with gold,” *Sci Rep*, no. 6, 2016, doi: 10.1038/srep38647ï.

CURRICULUM VITAE

Name Surname :Erhan Saatçioğlu
Place and Date of Birth :
E-Mail :

EDUCATION:

B.Sc. : 2019, Istanbul Medipol University, Biomedical Engineering

PROFESSIONAL EXPERIENCE AND REWARDS:

- 2017-2018 Honorary Student, Istanbul Medipol University
- 2016-2017 Honorary Student, Istanbul Medipol University
- 2015-2016 Honorary Student, Istanbul Medipol University